JOURNAL OF GEOPHYSICAL RESEARCH, VOL. 113, D14215, doi:10.1029/2007JD009774, 2008

Click Here for Full Article

Modeling the influence of aerosols on cloud microphysical properties in the east Asia region using a mesoscale model coupled with a bin-based cloud microphysics scheme

Takamichi Iguchi,[1] Teruyuki Nakajima,[1] Alexander P. Khain,[2] Kazuo Saito,[3] Toshihiko Takemura,[4] and Kentaroh Suzuki[5]

Received 31 December 2007; revised 29 March 2008; accepted 23 April 2008; published 29 July 2008.

[1] A bin-based microphysics scheme for cloud is implemented into a three-dimensional nonhydrostatic model and off-line coupled with a global aerosol transport model to reproduce realistic and inhomogeneous condensation nuclei (CN) fields. This coupling makes it possible to calculate cloud microphysical properties over a larger area under more realistic environmental conditions. Using the model, nested grid simulations are performed for two precipitation events associated with transitional synoptic-scale forcing during the spring over an area of the East China Sea. The nested grid simulations reproduce the general features of the horizontal distributions of variables such as effective droplet radius derived from satellite data retrieval. Comparison of the relationships among simulated cloud variables with those among satellite-derived variables reveals that the implementation of an inhomogeneous CN field results in a more accurate simulation of the distribution of cloud microphysical properties. Sensitivity tests with respect to CN concentration show that the simulated area and amount of precipitation are slightly affected by the CN concentration. Comparative simulations using bin-based and bulk microphysical schemes indicate that the difference in cloud microphysics has little effect on precipitation except over the areas of elevated pollution (i.e., elevated CN). Comparison with previous reports indicates that the precipitation response to aerosols is dependent on the environmental conditions and the type of the cloud system.

Citation: Iguchi, T., T. Nakajima, A. P. Khain, K. Saito, T. Takemura, and K. Suzuki (2008), Modeling the influence of aerosols on cloud microphysical properties in the east Asia region using a mesoscale model coupled with a bin-based cloud microphysics scheme, *J. Geophys. Res.*, *113*, D14215, doi:10.1029/2007JD009774.

1. Introduction

[2] Cloud droplets are formed through the condensation of water vapor around hydrophilic aerosols at low supersaturation in the troposphere. Such aerosols are referred to as cloud condensation nuclei (CCN) [*Pruppacher and Klett*, 1997]; a change in the concentration and characteristics of CCN can affect the properties of cloud as a colloidal suspension mass of droplets. A well-known example illustrating this relationship is the systematic difference in cloud properties between continental and ocean regions associated with large differences in aerosol concentrations [e.g., *Squires*, 1956]. The concentration and characteristics of CCN are therefore among the key factors controlling the microphysical and dynamical structures of cloud. It is consequently important to study the effect of aerosols on large-scale cloud dynamics and precipitation [*Ramanathan et al.*, 2001].

[3] The influence of changes in tropospheric aerosol concentration on the optical properties of cloud and precipitation efficiency is an important aspect of studies on cloud microphysics. *Twomey* [1974] pointed out that an increase in aerosol concentration produces an increase in cloud droplet number concentration (CDNC) assuming no change in the liquid water path (LWP). The possibility that an increase in anthropogenic aerosols may cause global cooling was also suggested. *Albrecht* [1989] found that a decrease in mean droplet radius caused by an increase in CDNC inhibits the growth of droplets through coagulation, thereby suppressing the generation of large droplets such as drizzle and rain particles. This process has the effect of extending cloud lifetime, resulting in an increase in the total global LWP and the fraction of cloud to drive significant global cooling.

[4] Characteristic cloud microphysics has been elucidated from satellite-derived variables such as cloud optical thickness (COT) and effective particle radius, and from the

[1] Center for Climate System Research, University of Tokyo, Kashiwa, Japan.
[2] Department of Atmospheric Sciences, Institute of Earth Sciences, Hebrew University of Jerusalem, Jerusalem, Israel.
[3] Meteorological Research Institute, Tsukuba, Japan.
[4] Research Institute for Applied Mechanics, Kyushu University, Fukuoka, Japan.
[5] Department of Atmospheric Science, Colorado State University, Fort Collins, Colorado, USA.

Copyright 2008 by the American Geophysical Union.
0148-0227/08/2007JD009774$09.00

relationships among these variables [e.g., *Han et al.*, 1994; *Nakajima and Nakajima*, 1995; *Rosenfeld and Lensky*, 1998; *Kawamoto et al.*, 2001]. Many studies have captured distinct signatures for aerosol-perturbed cloud. For example, an analysis of Advanced Very High Resolution Radiometer (AVHRR) data by *Nakajima and Nakajima* [1995] in a study of the characteristic features of cloud microphysics over the west coast of California revealed large-scale modification of cloud microphysics due to interaction with polluted air from the continent. *Rosenfeld* [2000] reported satellite-retrieved images of unperturbed cloud (composed of large droplets) and modified cloud (small droplets). Some general circulation models (GCMs) also now have the capacity to reproduce the observed effects of aerosols on cloud characteristics [e.g., *Lohmann*, 2002; *Penner et al.*, 2002; *Takemura et al.*, 2005]. However, the residence times of aerosols and cloud are too short and the distributions too temporally and spatially variable to be accurately simulated by the simplified parameterizations used in GCMs, and the indirect effects of aerosols are highly dependent on the parameterization. It was concluded in the *Intergovernmental Panel on Climate Change* [2007] report that the radiative forcing of the cloud albedo effect (Twomey effect or first indirect effect) by anthropogenic aerosols is -0.7 W m^{-2}, varying widely from -0.3 to -1.8 W m^{-2} at the top of the atmosphere. It was also stressed in the report that the low level of scientific understanding of this process remains an issue. Direct modeling of the interaction between aerosols and cloud through high-resolution simulations using regional-scale models therefore remains of considerable importance.

[5] Two microphysical approaches are generally adopted to describe cloud microphysical processes; a bulk approach and a bin approach. Models based on the bulk microphysical approach predict integrated values such as mass content (one-moment schemes), or content and number concentration (two-moment schemes), and the size distributions of hydrometeors are assumed to be given. In the bin microphysical approach, the size distributions of cloud hydrometeors are approximated discretely by a number of size bins, offering the key advantage of allowing the calculation of size distributions in consideration of aerosol properties, which is an important factor in the modeling of indirect aerosol effects. Using the binned size distributions, it is possible to calculate the number concentration, mean radius, and total volume of hydrometeors, which are important parameters in determining the radiation properties, the residence times of cloud, and precipitation efficiency.

[6] Most spectral bin models have been executed as two-dimensional simulations [e.g., *Arnason and Greenfield*, 1972; *Takahashi*, 1974; *Khain and Sednev*, 1996; *Khain et al.*, 2000, 2004], incurring large computation cost. The early three-dimensional models were generally warm rain models that exclude ice processes [e.g., *Kogan*, 1991]. More recent models running on massive computational servers, however, can now account for ice processes [e.g., *Takahashi and Shimura*, 2004]. Bin models have been employed in a number of studies to investigate the effects of aerosols on cloud microphysics [e.g., *Khain et al.*, 1999], the dynamics of deep convection, and stratocumulus cloud [e.g., *Feingold and Kreidenweis*, 2002], as well as in the investigation of aqueous chemistry [e.g., *Chen and Lamb*, 1994]. In most prior studies using bin models, however, simulations have been performed assuming a simple scenario such as a horizontally uniform initial condition with an idealized convection or disturbance. Although high-resolution simulations of this type have successfully reproduced the dynamical and microphysical structures of an individual cloud or cloud clusters, the structures remain heavily dependent on the assumption of the initial and boundary conditions, as well as the initial disturbances applied for convection triggering. The results may therefore be unsuitable for comparison with observations under real and complex conditions. Bin model simulations reproducing the cloud field under realistically complex conditions are thus expected provide invaluable information, even if some of the benefit of high-resolution simulations is sacrificed because of computational limitations.

[7] Numerical weather prediction (NWP) models executed as nested grid simulations are a suitable class of model for three-dimensional bin model simulations. *Lynn et al.* [2005a, 2005b] developed a fast version of the microphysical module package of the Hebrew University cloud model (HUCM) [*Khain and Sednev*, 1996, *Khain et al.*, 1999, 2000, 2004], and implemented it into a nonhydrostatic mesoscale modeling system known as the fifth-generation Pennsylvania State University–National Center for Atmospheric Research (Penn State–NCAR) Mesoscale Model (MM5) [e.g., *Dudhia*, 1993; *Grell et al.*, 1994]. A comparison of simulated cloud and precipitation over Florida on 27 July 1991 with the output of a bulk model simulation revealed important advantages of the bin approach. Similar to prior studies [e.g., *Khain et al.*, 2000], an initially horizontally uniform concentration was employed for condensation nuclei (CN; all soluble and activatable aerosol particles, following the definitions of *Pruppacher and Klett* [1997, chapter 9]), although the dynamical field was initialized using reanalysis or outer model data. The results reported by *Lynn et al.* [2005a, 2005b, 2007] indicated that the bin approach provides a superior prediction of precipitation and reproduces a more realistic cloud structure compared to the bulk model. However, the simulation domain was relatively small (e.g., 300 km $\times$ 270 km [*Lynn et al.*, 2005b]), and the simulations were performed for a relatively short period.

[8] In the present study, the scheme with bin microphysics for cloud in the HUCM [*Khain et al.*, 2000] is integrated into a three-dimensional nonhydrostatic model (NHM) developed by the Numerical Prediction Division (NPD) of the Japan Meteorological Agency (JMA) in partnership with the Meteorological Research Institute (MRI) known as the JMA-NHM [e.g., *Saito et al.*, 2006]. The implemented model can be used to perform nested grid simulations of realistically complex conditions, including initial fields and lateral boundary conditions prepared by interpolation of a precalculated field of the outer model or reanalysis data. Note that this nesting procedure is also applicable to the field of aerosol concentrations given from a global run of an aerosol transport model, providing a means of introducing a realistic and inhomogeneous CN distribution. The microphysical variables of cloud, such as the effective droplet radius, are calculated directly by integrating the binned size distribution. These variables can be directly compared with satellite data, taking into account that the remotely sensed variables pertain to heights corresponding to one unit

optical depth below the cloud top [*Nakajima and King*, 1990].

[9] Using the proposed model, cloud fields with detailed cloud microphysics are simulated in the present study for 2 days during spring over a region of the East China Sea, and the simulated cloud properties are compared with satellite observations. The sensitivity of cloud dynamics and precipitation to changes in the CN concentration are also investigated using this model.

[10] The description of the model is reported in section 2, and the setup and results of numerical experiments and comparisons with observations are presented in section 3. Summary and conclusions are finally given in section 4.

2. Model Description

2.1. Dynamics

[11] The main dynamics framework is that provided by the operational version of the JMA-NHM, which employs fully compressible nonhydrostatic equations as basic governing equations [*Saito et al.*, 2001, 2006]. In the JMA-NHM, two schemes are available for the inhibition of sound wave inflation, which restricts the maximum time step: a scheme that treats waves implicitly in both the horizontal and vertical directions (HI-VI scheme), and a scheme that treats waves explicitly in the horizontal direction and implicitly in the vertical direction (HE-VI scheme). As there are difficulties in solving the Helmholtz-type pressure tendency equation of the HI-VI scheme in a multiprocessor environment, the HE-VI scheme is employed in the present simulations. The Arakawa-C and Lorentz grid structures are adopted for the horizontal and vertical grid configurations, respectively. The surface boundary layer dynamics are calculated using the Monin and Obukhov similarity theory, and a four-layer soil model is employed to calculate ground temperature. A 1.5-order turbulent closure model is applied to calculate turbulent diffusion coefficients, and a fourth-order linear damping scheme is applied to prevent the development of computation-derived noise.

2.2. Cloud Microphysics

[12] The original version of the JMA-NHM applies a scheme with explicit two-water and three-ice, bulk microphysics [*Ikawa and Saito*, 1991; *Yamada*, 2003]. This scheme has been replaced in the present study by a new bin microphysics scheme based on the cloud microphysical module package of the HUCM [*Khain and Sednev*, 1995, 1996; *Khain et al.*, 2000]. The scheme treats one water and 6 ice hydrometeor types: water droplets, ice crystals (plate, column, dendrite), snowflakes, graupel, and hail. The characteristics of hydrometeor particles, such as particle shape and bulk density, are set according to the values given by *Khain and Sednev* [1995]. The size distribution functions of hydrometeors are represented on a grid containing 33 doubling mass bins covering particles sizes (melted radii) in the range 2.0 μm $< r <$ 3251 μm. Formulae describing nucleation for droplets and ice crystals, condensation and deposition growth, evaporation, sublimation, droplet freezing, melting, and coalescence growth are given in Appendix A. The terminal velocities for each size bin of hydrometeors are determined on the basis of the mass, hydrometeor type, and air density [*Khain and Sednev*, 1995, 1996]. The thickness of the lowest vertical layer is set to 40 m, which is considered sufficiently small to represent the atmospheric boundary layer in mesoscale simulations. Whereas the Eulerian scheme is adopted in the original HUCM to compute the gravitational sedimentation of hydrometeors, the use of a narrow layer imposes strong demands on the time step to adhere to the Courant-Friedrichs-Lewy (CFL) condition. In the present model, a box-Lagrangian raindrop scheme [*Kato*, 1995], developed in JMA-NHM for the framework of the bulk microphysical scheme, is employed to avoid the restriction by the CFL condition. The coupling of the bin microphysical scheme to the box-Lagrangian scheme is described in Appendix A. The subgrid convective parameterization scheme in the original version of the JMA-NHM is not applied in the present simulations because no parameterization has been implemented for bin microphysics for cloud.

2.3. Treatment of Condensation Nuclei

[13] In the original version of the HUCM, the size distribution function for CN is discretized into a number of size bins, with the number concentration in each bin acting as a prognostic variable; the advection, diffusion, and activation (nucleation to water droplets) of CN at supersaturation are calculated at every time step. The same treatment is employed in the bin scheme implemented in the JMA-NHM. The present model applies a CN mass grid containing 13 bins with a radius range from 10^{-3} μm to 1 μm, in contrast to the 33 bins defined in the HUCM. The use of a smaller number of bins improves the efficiency of computation. Aerosols with radius smaller than 10^{-3} μm are not usually activated to droplets and can be safely omitted.

[14] In prior studies using the HUCM, the initial CN concentration field is defined by an exponential decrease with height and horizontal uniformity. At the lateral boundaries, zero horizontal gradients are assumed. Other prior studies involving bin schemes have adopted similar initializations and lateral boundary conditions in terms of CN concentration [e.g., *Kogan*, 1991; *Lynn et al.*, 2005a, 2005b]. In the present model, an inhomogeneous initial field and a temporally variable lateral boundary condition are defined for CN concentration by introducing the nesting procedure described above. This implementation is an important advancement over previous studies. Interpolation in the nesting procedure is applied to the field of aerosol concentration given by a global numerical simulation using the spectral radiation transport model for aerosol species (SPRINTARS) [*Takemura et al.*, 2000, 2002, 2005]. The SPRINTARS is coupled with the Center for Climate System Research/National Institute for Environmental Studies Atmospheric General Circulation Model (CCSR/NIES-AGCM) [*Numaguti et al.*, 1995]. Five tropospheric aerosols (organic carbonaceous, black carbonaceous, soil dust, sulfate, and sea salt aerosols) are introduced into the SPRINTARS simulation. Among these aerosols, organic carbonaceous, sulfate, and sea salt aerosols are assumed to be hygroscopic particles and hence CN, which acts as potential CCN. The concentration of each hygroscopic aerosol is provided by the SPRINTARS simulation in the form of a bulk number concentration of dry particles, which is converted to a size distribution of CN in an initial field

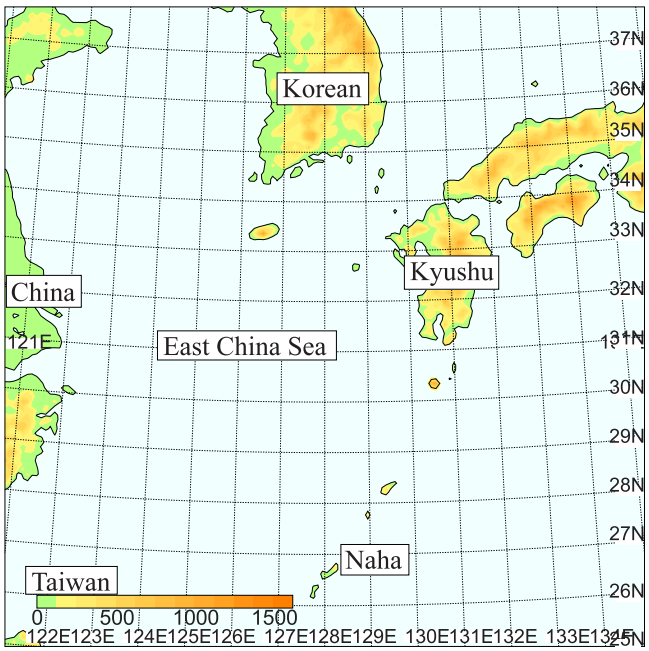

Figure 1. Simulation domain, projected on a map of Lambert coordinates. Horizontal domain is 1400 km × 1400 km in size. Contours denote orography.

and a temporally variable boundary condition in the implemented model. A size distribution is assumed for each aerosol type. This off-line coupling with the SPRINTARS simulation is summarized in Appendix B.

2.4. Atmospheric Radiation

[15] The broadband radiative transfer code "mstrn-x" developed by the CCSR [*Nakajima et al.*, 2000; M. Sekiguchi and T. Nakajima, The study of the absorption process and its computational optimization in an atmospheric general circulation model, submitted to *Journal of Quantitative Spectroscopy and Radiative Transfer*, 2008] for the CCSR/NIES-AGCM was implemented in the JMA-NHM by H. Miura (manuscript in preparation, 2008). This scheme differs from that originally provided in the JMA-NHM. The mstrn-x applies a k distribution approximation and two-stream delta-Gaussian scheme to calculate radiative fluxes accounting for line and continuum absorption/emission, as well as multiple scattering by atmospheric molecules (H_2O, CO_2, O_3, N_2O, CH_4, and O_2) and aerosol and cloud particles. The radiative transfer calculation is performed in k distribution channels of 18 wavelength bands over the spectral region from 0.2 μm to 200 μm. Optical parameters for particulate matter (i.e., extinction and absorption coefficients, moments of the volume scattering phase function), which are dependent on radii and optical characteristics, are formulated so as to allow computation of the optical thickness and single scattering albedo of aerosols and cloud.

[16] The present version of mstrn-x has been extended to work with both the previous bulk model and the newly implemented bin cloud microphysics model. When using the scheme with bin microphysics for cloud, the mode radius of hydrometeors is variable and calculated explicitly, allowing the calculation of optical parameters to include the species and mode radius of each hydrometeor. The mstrn-x code originally implemented in CCSR/NIES-AGCM can treat radiation processes by chlorofluorocarbons (CFCs), halocarbons, and aerosol particles. These computations are omitted in the mstrn-x module of the present model so as to reduce computational cost. The radiation process for aerosol particles is excluded because the optical properties of aerosols become undefined in the nesting procedure for the CN field.

3. Results

3.1. Setup of Numerical Experiments

[17] Numerical simulations were performed for a region of the East China Sea. The simulation domain has a horizontal scale of 1400 km and is centered on the sea west of Kyushu, Japan (Figure 1). This area was selected because of the availability of good observational data sets for this region, as acquired by the Asian Atmospheric Particulate Environment Change Studies (APEX) conducted as a Core Research Project for the Evolutional Science and Technology of the Japan Science and Technology Agency (CREST/JST) [*Nakajima et al.*, 2003].

[18] The JMA mesoanalysis data set (JMA-MANAL), with horizontal grid interval of 10 km, 20 vertical layers, and 4 samples per day, was employed for initialization and to set the lateral boundary conditions of dynamical variables, such as horizontal velocities, potential temperature, and the mixing ratio of water vapor. Sea surface temperature (SST) data were taken from the National Centers for Environmental Prediction (NCEP) Reanalysis data with a horizontal resolution of T62 Gaussian grid and 4 samples per day. The concentrations of hygroscopic aerosols were obtained from a global SPRINTARS simulation coupled with the CCSR/NIES-AGCM with a horizontal resolution of T106 Gaussian grid, 20 vertical layers, and 4 samples per day. These concentrations are introduced into the CN nesting procedure as described in section 2.3 and Appendix B.

[19] The horizontal grid size of the model was set at 7 km (202 × 202 grid points), and the vertical component to a height of 22600 m was divided into 40 layers with intervals increasing from 40 m to 1120 m with altitude. Terrain-following coordinates were applied [*Gal-Chen and Somerville*, 1975]. A time step of 20 s was set for simulation of dynamics, and a variable interval was applied for calculation of condensation, evaporation, deposition, and sublimation [*Khain and Sednev*, 1996]. The time steps for microphysical calculations are typically shorter for dynamics calculations. The use of coarse resolution without convective parameterizations is justified considering the targeted region and season, in that cloudiness is mainly associated with stratiform and frontal structures with large characteristic horizontal scales and comparatively low vertical velocities.

[20] The numerical experiments were conducted for 2 days with dissimilar weather conditions, 2 and 8 April 2003. Calculations were performed from 1800 universal time (UTC) of the previous day to 0300 UTC.

3.2. General Weather Conditions for Target Days

[21] Satellite weather imagery acquired by the Moderate Resolution Imaging Spectroradiometer on Terra (Terra/MODIS) is available for the target region at close to noon

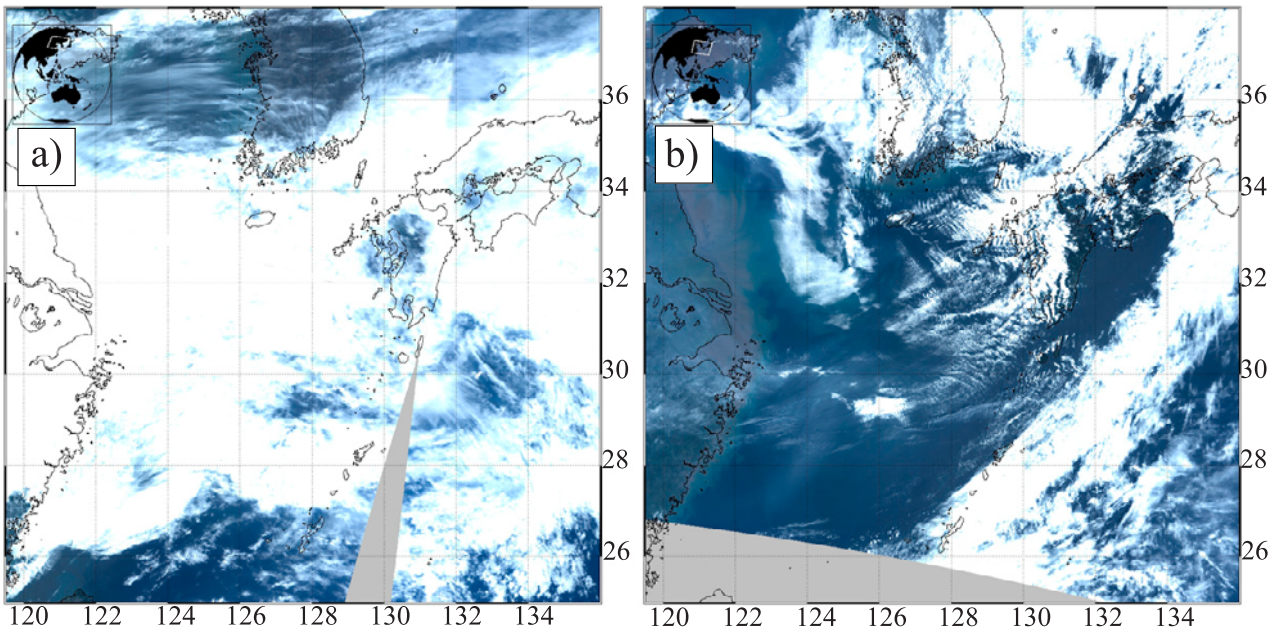

Figure 2. Terra/MODIS RGB images for (a) 2 April and (b) 8 April 2003.

(0300 UTC, 1200 JST) on the target days. Figure 2 shows the red, green, blue (RGB) satellite images. At 0000 UTC on 2 April, a low-pressure system was present with an associated stationary front extending east and west at a latitude of close to 30°N and into the sea south of Japan. The satellite image indicates that almost all parts of the area were covered by cloud: cirrus over the Korean Peninsula and the Japan Sea, large thick cloud on the east coast of China, and low cloud over the East China Sea around Kyushu Island. A synoptic westerly wind was dominant throughout the analysis domain, causing the pattern of cloud and precipitation to progress toward the east.

[22] On 8 April, a migrating extratropical low was located over the Japan Sea near the Korean Peninsula. A row of thick convective cloud had developed from the center of the Japan Sea to the Okinawa region and Taiwan attributable to a cold front associated with the low. Very thin cloud covering a wide region of the analysis domain can also be observed in the satellite image.

3.3. Spatial Distribution of CN Concentration on Target Days

[23] The simulation was performed using an inhomogeneous initial field and temporally variable lateral boundary condition in terms of CN concentration by introducing the CN nesting procedure described in section 2.3 and Appendix B; interpolation in the CN nesting procedure is applied to the field of hygroscopic aerosol concentrations given by the SPRINTARS coupled with CCSR/NIES-AGCM simulation. Figures 3 and 4 show the horizontal distributions of CCN column number concentrations at supersaturation of 0.3% (SS = 0.3%) in the initial fields of the nested grid simulation at 1800 UTC on 1 and 7 April, and in the prognosticated field under noncloud conditions (without cloud microphysics) at the same supersaturation at 0300 UTC on 2 and 8 April. The CCN number concentration at supersaturation was determined for each model grid point by taking the total number concentration of CN larger than the critical radius of CCN at supersaturation.

[24] On 2 April, the SPRINTARS simulation predicts an eastward propagation of a carbonaceous aerosol plume from southern China, resulting in a high CCN concentration at SS = 0.3% in the southern part of the analysis domain (Figure 3a). The high CCN concentration is transported without appreciable change by a westward inflow (Figure 3b). On 8 April, the CCN concentrations at SS = 0.3% varies markedly between the western and eastern parts of the analysis domain across the cold front (Figure 4a). The SPRINTARS simulation predicts high concentrations of both sulfate and carbonaceous aerosols bordering the cold front on the western side. The area of high CCN concentration progresses and extends eastward along with the cold front under the influence of the synoptic westerly wind (Figure 4b).

[25] The prognosticated CCN concentration is compared with in situ measurement concentrations recorded by a Cessna 404 aircraft during the APEX-E3 campaign (Figure 5). Given the relatively coarse resolution of the present simulations, a reasonably simple qualitative method is adopted for comparison. The observed CCN number concentrations are those at supersaturation in the chamber of the CCN counter onboard the aircraft, as measured using a CCN counter (ACN-1000, Sigmatec). The measurements during the APEX-E3 campaign have been reported by *Ishizaka* [2004], and the measurement methodology is the same as that reported by *Adhikari et al.* [2005], who reported aircraft observations targeting the same region in April 2001 during the APEX-E2/ACE-Asia campaign. The flight legs on 2 and 8 April 2003 fall predominantly within a domain within a radius of ±0.5° latitude and longitude centered at 129.5°E, 30.5°N. The flights on the 2 days were conducted from 0340 to 0615 UTC (2 April) and 0120 to 0420 UTC (April 8). Measured CCN concentrations were obtained at supersaturations in the ranges of 0.07–0.22% on

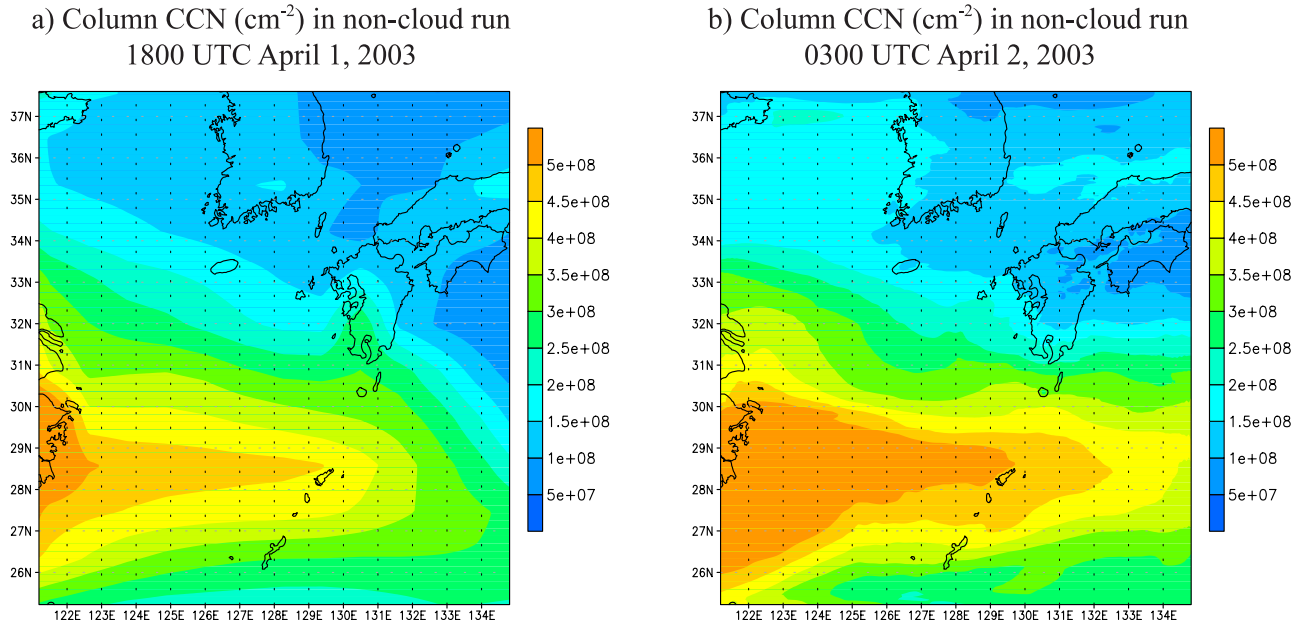

Figure 3. Simulated horizontal distributions of CCN column number concentration (cm^{-2}) at supersaturation of 0.3% in a noncloud run at (a) 1800 UTC 1 April and (b) 0300 UTC 3 April 2003.

2 April and 0.09–0.32% on 8 April (supersaturation in the chamber varying irregularly). CCN concentrations were recorded at approximately 1 min intervals throughout the flight, which was conducted mainly outside cloud but also partially inside cloud. The simulated CCN concentrations are those calculated using the CN size distributions prognosticated by a noncloud run (without cloud microphysics) and by a standard run (bin microphysics for cloud) of the JMA-NHM, and are provided as horizontally averages over a domain within a radius of ±0.5° latitude and longitude centered at 129.5°E, 30.5°N at 0300 UTC on each day. The simulated CCN concentrations were determined at SS = 0.1% on 2 April, and SS = 0.2% on 8 April, close to the mean values obtained in the measurements. The noncloud run was executed to show the CCN concentration without consumption followed by the formation of cloud. Note that the droplet number concentration generated by activation (nucleation) at SS < 0.1% on 2 April and SS < 0.2% on 8 April in the standard run is equal to the difference between the plotted CCN concentrations of the standard and noncloud runs. The large error bars at altitudes at which the standard and noncloud runs diverge reflects the activation of

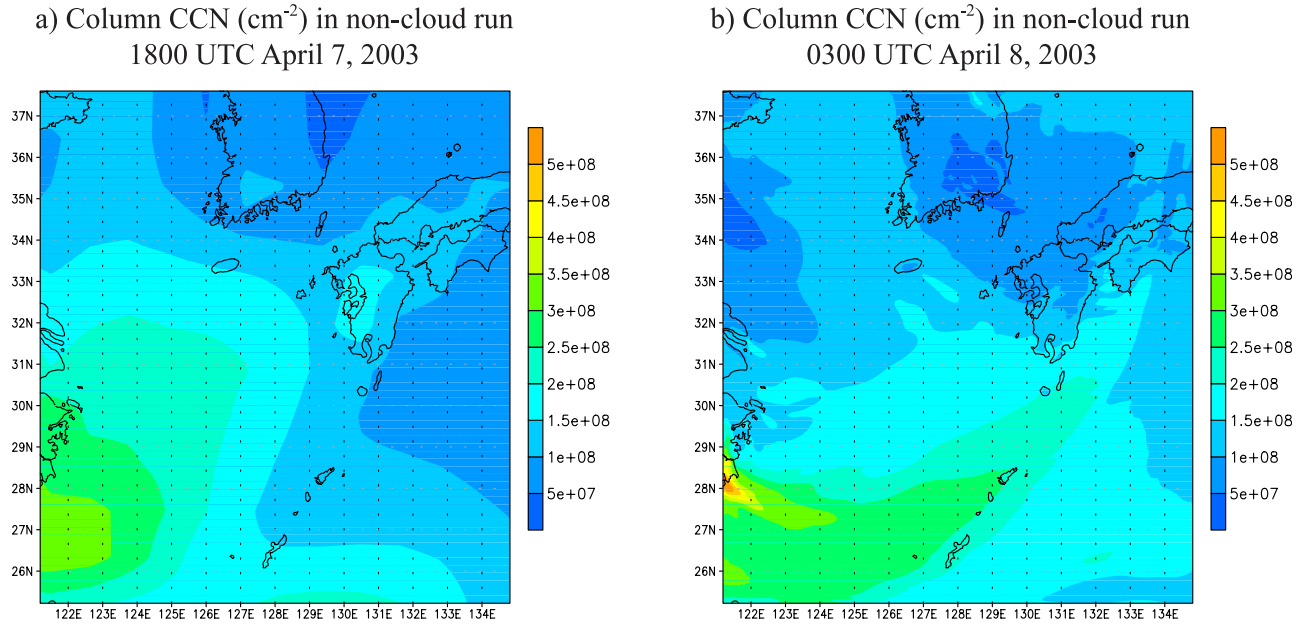

Figure 4. Simulated horizontal distributions of CCN column number concentration (cm^{-2}) at supersaturation of 0.3% in a noncloud run at (a) 1800 UTC 7 April and (b) 0300 UTC 8 April 2003.

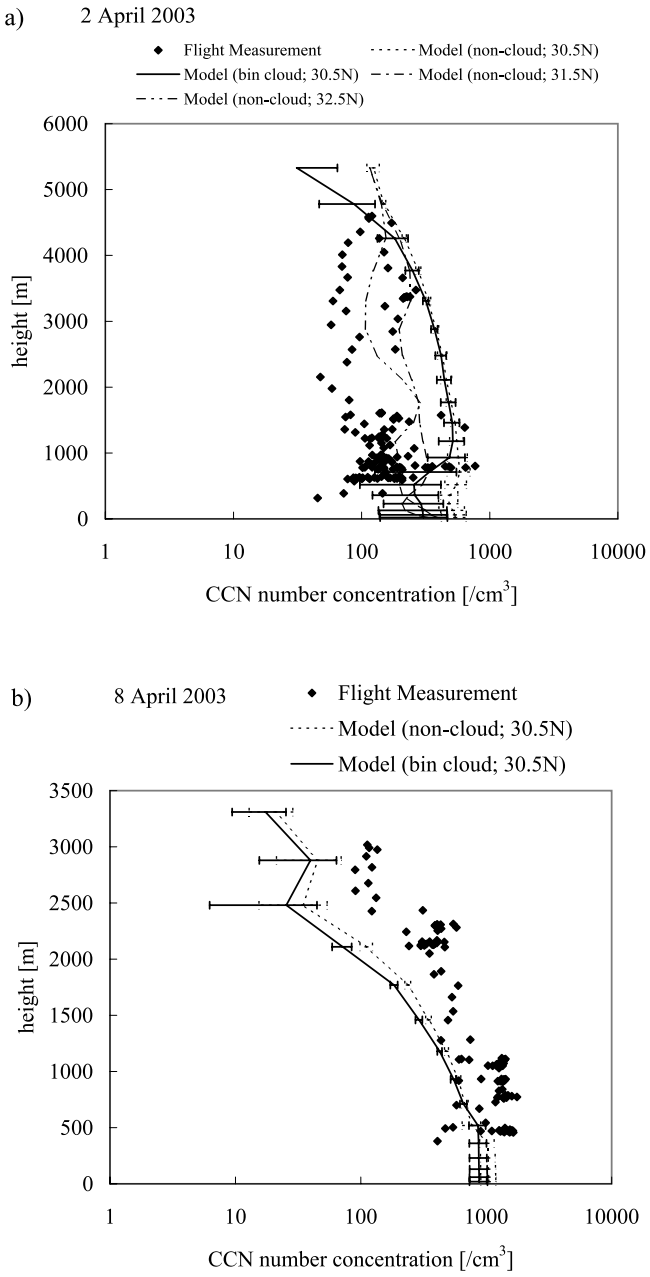

Figure 5. Vertical distribution of CCN number concentration (cm^{-3}) at various levels of supersaturation on (a) 2 April and (b) 8 April 2003. Dots denote aircraft observations at supersaturation of 0.07–0.22% (Figure 5a) and 0.09–0.32% (Figure 5b). Dashed and solid lines denote horizontally averaged concentrations given by the noncloud and standard runs in a domain of radius ±0.5° centered at 129.5°E, 30.5°N (supersaturation, 0.1% (Figure 5a) and 0.2% (Figure 5b)). Dashed-dotted and dash-double-dotted lines denote corresponding simulations for domains centered at 31.5°N and 32.5°N on the same 129.5°E line.

CN in cloud, which results in a large horizontally variation in CCN concentration. A certain degree of uncertainty in the comparison of aircraft data recorded in cloud and noncloud space is unavoidable because of the simple sampling method and the coarse resolution of the present JMA-NHM simulation.

[26] As shown in Figure 5, the simulations reasonably reproduce the observed vertical profiles of CCN concentration and the difference in these profiles between the two target days. On 2 April (Figure 5a), higher concentrations occur at high altitude compared to the concentrations at the lower boundary layer because of the uplift of layered aerosol plumes by convection. On 8 April (Figure 5b), the predicted CCN concentrations follow a log linear decrease with altitude, as similarly observed in the measured profile. The CN concentration generated in the simulations thus appears to reproduce the main factors of aerosol effects on the optical and microphysical properties of cloud in these two periods.

[27] The horizontal resolution of the SPRINTARS simulation is defined by a T106 Gaussian grid, corresponding to approximately 1.125°. This relatively coarse resolution limits the accuracy of prediction using the CN nesting procedure on a regional scale, and the associated error in the CN horizontal distribution can result in remarkable error in simulated CCN concentrations compared with observations. In Figure 5a, the simulation can be seen to overestimate the CCN concentration in a region of ±0.5° in radius centered at 129.5°E, 30.5°N on 2 April. The average CCN concentrations in domains of the same radius centered at 31.5°N and 32.5°N (129.5°E) are in better agreement with the flight measurements. In the region centered at 129.5°E, 30.5°N, a distinct north–south gradient is apparent in the simulated spatial distribution of CN concentration (Figure 3b), and the simulated CCN concentrations vary considerably around this point.

[28] Although it may appear more valid and realistic to apply the observed CN and CCN concentrations directly for initialization of the model, direct measurements of CN and CCN through surface and aircraft observations are spatially and temporally sparse. The observational data set is also unsuitable for application of the CN nesting procedure because of the spatial and/or temporal nonuniformity of the data set. Using the uniform and complete simulated hygroscopic aerosol and hence CN concentrations allows the bin model to be executed for all regions and times using the CN nesting procedure.

[29] The prognostication of CN concentration by the present model includes uncertainty associated with the assumption of size distribution functions, the relatively coarse horizontal resolution of the global aerosol transport model, and the omission of scavenging due to Brownian diffusion or inertial collision between CN and hydrometeors in the bin model. The size distribution functions assumed for conversion of bulk aerosol number concentrations given by the SPRINATARS simulation into the size distribution of CN (see Appendix B) will have a strong influence on the CCN concentration at supersaturation. Although fixed size distribution functions are assumed to be given, there is a spatial variation in an actual size distribution of aerosols. For example, existence of very small particles in the free atmosphere was reported by several studies [e.g., *Clarke and Kapustin*, 2002; *Menzies et al.*, 2002]. The coarse horizontal resolution will limit the accuracy of prediction on the present scale; and simplification of omitting scav-

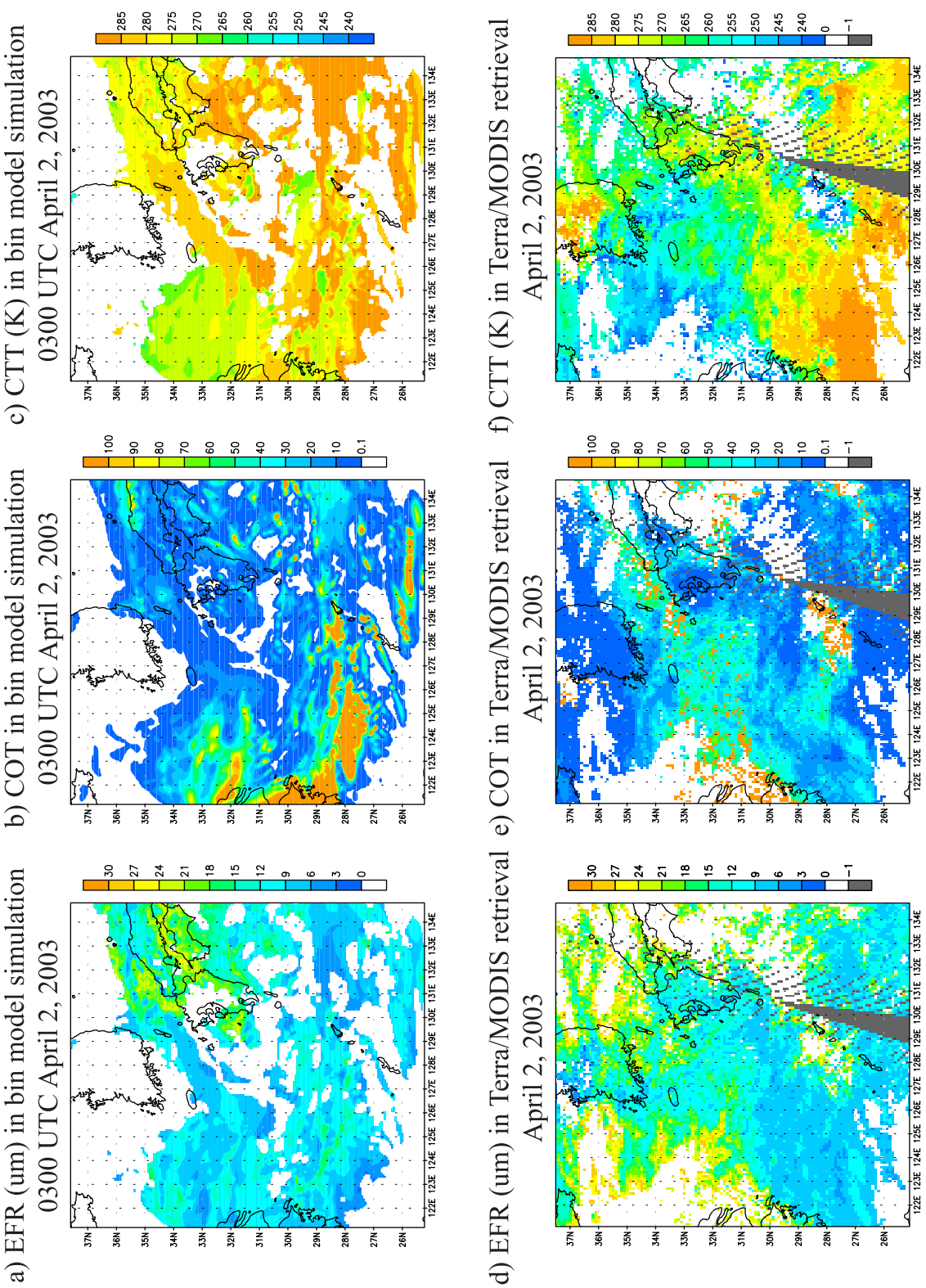

Figure 6. (a–c) Simulated horizontal distributions and (d–f) Terra/MODIS retrievals of effective droplet radius (μm) near the cloud top (Figures 6a and 6d), COT (Figures 6b and 6e), and cloud top temperature (K) (Figures 6c and 6f) at 0300 UTC on 2 April 2003.

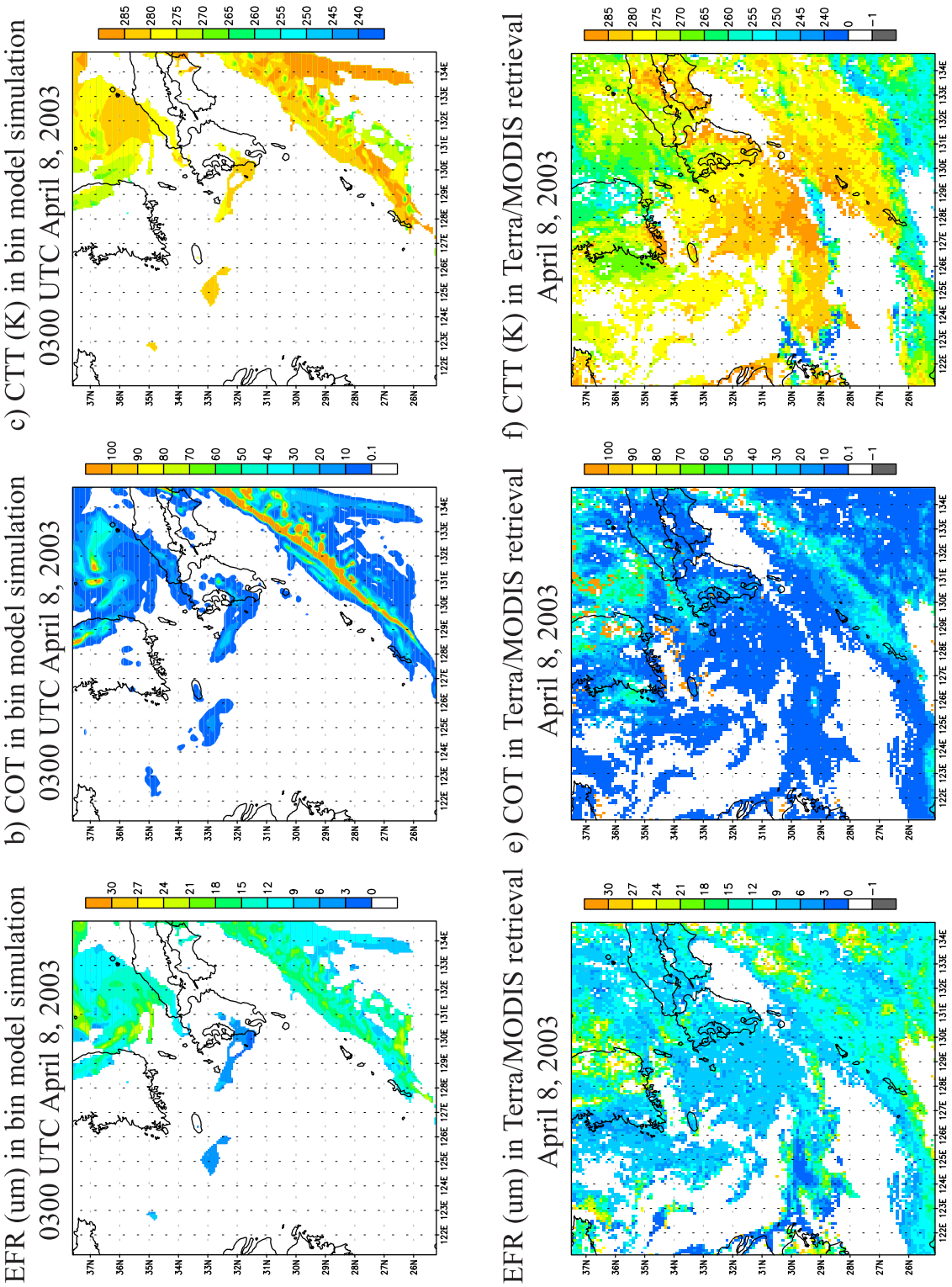

Figure 7. (a–c) Simulated horizontal distributions and (d–f) Terra/MODIS retrievals of effective droplet radius (μm) near the cloud top (Figures 7a and 7d), COT (Figures 7b and 7e), and cloud top temperature (K) (Figures 7c and 7f) at 0300 UTC on 8 April 2003.

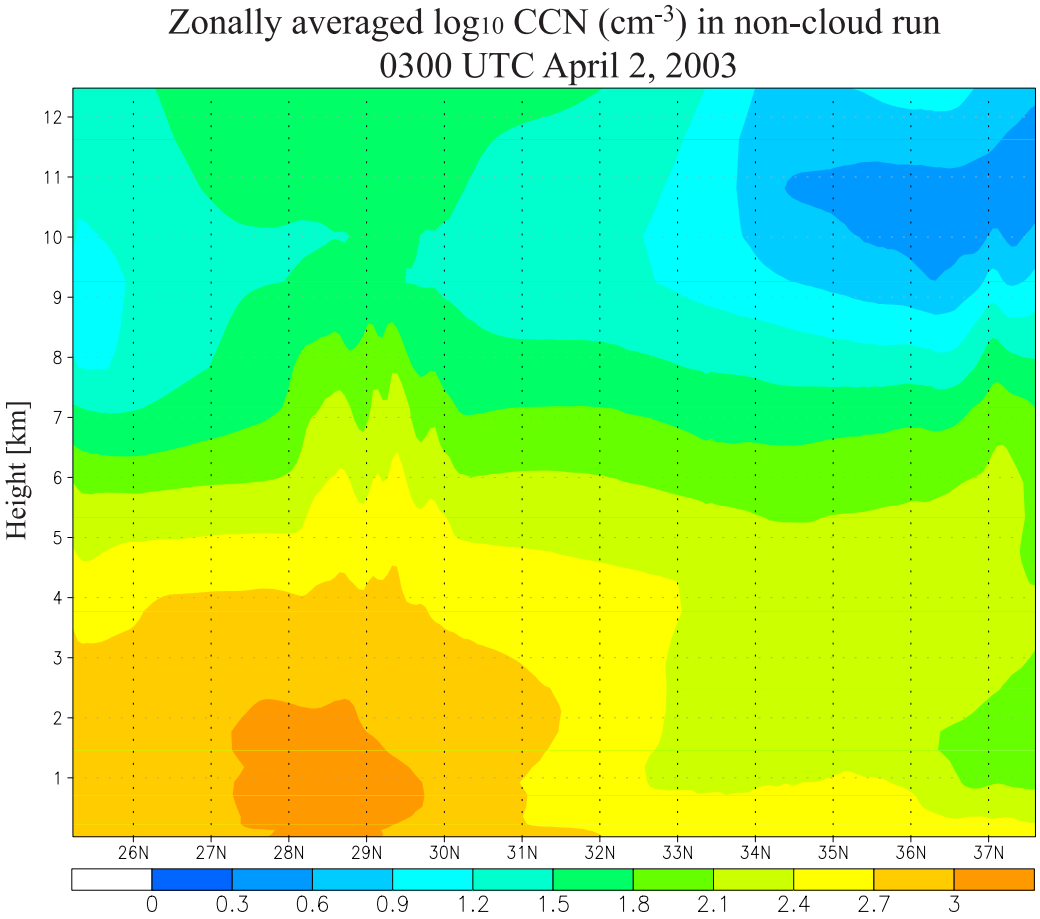

Figure 8. Latitude-height cross section of zonally averaged logarithmic CCN concentration (cm^{-3}) at supersaturation of 0.3% for the noncloud run at 0300 UTC on 2 April 2003.

enging may introduce additional error into the simulated CN concentrations.

3.4. Comparison With Terra/MODIS Observations

[30] Figures 6 and 7 compare the horizontal distributions of simulated and Terra/MODIS-derived cloud variables (effective droplet radii around cloud top, COT, and cloud top temperature) at 0300 UTC on 2 and 8 April. The satellite-based water cloud information was obtained by applying the algorithm of *Nakajima and Nakajima* [1995] and *Nakajima et al.* [2005] to Terra/MODIS data. As the remotely sensed effective droplet radius and cloud top temperature are representative of altitudes near the cloud top [*Nakajima and King*, 1990], the corresponding model values are evaluated at the grid points at which the COT for the top of the atmosphere is 30% of the total COT in the column [*Suzuki et al.*, 2006].

[31] The effective droplet radius (r_e) is calculated by

$$r_e = \frac{\int_{r\,\min}^{r\,\max} rn(r)\pi r^2 \mathrm{d}r}{\int_{r\,\min}^{r\,\max} n(r)\pi r^2 \mathrm{d}r}, \tag{1}$$

where r is the cloud droplet radius, $n(r)$ is the number size distribution of cloud droplets, and r_{min} and r_{max} are the threshold radii in the droplet bins. In the present model, r_{min} = 2 μm and r_{max} = 32 μm, corresponding to the radii of the 1st and 13th droplet bins. The value of r_{max} was decided on the basis of the sensitivity of the Terra/MODIS sensor. The COT is calculated by [*Stephens*, 1978]

$$\tau = Q_{ext} \int_0^H \int_{r\,\min}^{r\,\max} \pi r^2 n(r) \mathrm{d}r \mathrm{d}z, \tag{2}$$

where H is the height of the top of the atmosphere in the simulation and Q_{ext} is the mean scattering efficiency. In the present study, Q_{ext} = 2 is assumed as a large-particle approximation.

[32] Comparison between Figures 2a and 6 reveals that some regions of cloud are excluded from the Terra/MODIS analysis, because of the assignment of cloud in the regions, e.g., centered around 133°E and 122°E on the 33°N line, as ice cloud in the cloud retrieval algorithm. In all other regions, the simulation satisfactorily reproduces the magnitude and distribution of each variable determined from the Terra/MODIS data. In Figure 6, the simulated cloud top temperatures can be seen to be generally higher than the corresponding satellite-based temperatures, particularly around the Japan Islands. The extent of cloud in the East China Sea in the simulations is smaller than that indicated by observations. On 8 April (Figure 7), the simulation reproduced the cloud row due to the cold front as observed

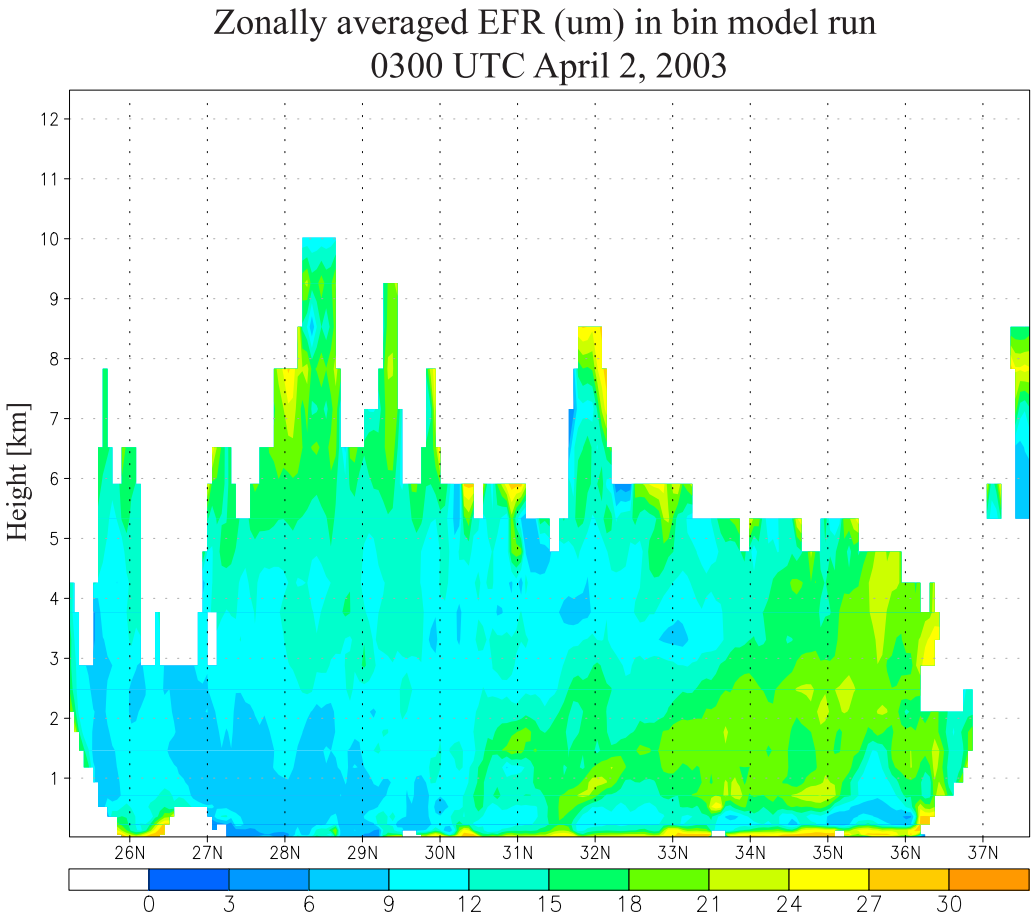

Figure 9. Latitude-height cross section of zonally averaged effective droplet radius (μm) in bin cloud microphysics run at 0300 UTC on 2 April 2003.

by satellite, apart from the very thin cloud covering a wide area of the analysis domain. The agreement with satellite-based data for 8 April is better than for 2 April, with more accurate reproduction of cloudiness on the 8 April. The distributions of simulated variables for thick cloud are in better agreement with the satellite-based observations, reflecting the effect of the coarse model resolution, which is less suitable for resolving small clouds.

[33] Figure 8 shows the latitude-altitude cross section of zonally averaged CCN concentration at SS = 0.3% for the noncloud (without cloud microphysics) run at 0300 UTC on 2 April. The CCN is concentrated in the southern part of the domain, as also found in Figure 3. Figure 9 shows the corresponding cross section of zonally averaged effective droplet radius obtained in the standard run. The effective radius is smaller in the lower layer of the southern part of the domain because of the elevated CCN concentration in that region, while the relatively large effective radius in the region from 34°N to 36°N is associated with the lower CCN concentration in this latter region. A close relationship between cloud microphysics (effective droplet radius) and CCN concentration is thus resolved by the present model even at the large scales considered in this study.

[34] The temperature/effective radius (T–r_e) relationship between the cloud top temperature and the effective droplet radius around the cloud top is an important aspect of cloud microphysics. The variation among vertical T–r_e profiles can be explained as being due to local variations in CN concentration [e.g., *Rosenfeld and Lensky*, 1998; *Rosenfeld*, 2000]. Figure 10a shows T–r_e profiles for the case shown in Figure 6 (2 April). These T–r_e relations are plotted separately for the northern and southern regions, partitioned at 31.5°N for both the simulated and Terra/MODIS-derived variables. The T–r_e relation for warm cloud in the lower layer represented relatively well despite some overestimation of the effective droplet radii, whereas the relation for supercooled droplets in mixed phase cloud is poorly simulated in this case. As the boundary between the lower and upper layers is roughly located at 273 K, cloud in the lower should consist of liquid phase cloud air mass, while cloud in the upper layer should consist of a mixed phase cloud air mass. In the upper layers, there is little difference between the simulated northern and southern T–r_e relations, whereas a distinct difference is apparent between the observed northern and southern relations (except in the top layers at <260 K). The satellite-derived effective droplet radius increases through the layer with decreasing cloud top temperature, whereas the simulated effective radius decreases in the upper layer.

[35] A characteristic common to both the simulated and observed T–r_e relations is the smaller effective droplet radii in the southern part of the lower layer compared to the northern part. This north–south change is considered to be due to the change in CN concentration. For confirmation of

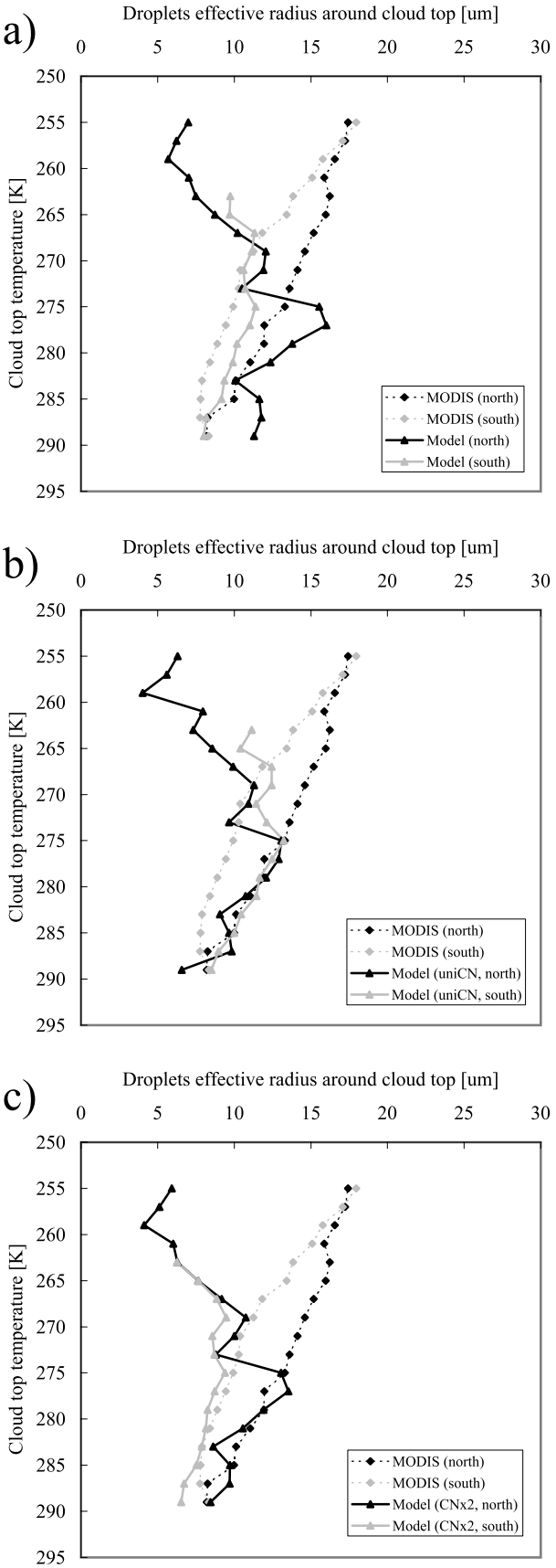

this relationship, an additional simulation run was performed with uniform horizontal average CN concentration at each level and at each time (Figure 10b). In this case, the simulated $T-r_e$ relations for the northern and southern parts are largely identical. The spatial change in CN concentrations is therefore primarily responsible for the spatial change in the simulated $T-r_e$ relations. Prediction of the spatial distribution of CN concentration using the CN nesting procedure is therefore necessary in order to introduce the spatial distribution of cloud microphysics indicated by satellite imagery.

[36] A supplemental run was performed with doubled CN concentrations in all bins over the entire domain (Figure 10c). The observed $T-r_e$ relations for the lower layers are in better agreement with the doubled run than the standard run, and it is clear that an increase in CN concentration leads to a decrease in simulated effective droplet radius. This result also suggests that the CN concentration in the standard run was underestimated.

[37] In previous studies [*Han et al.*, 1994; *Nakajima and Nakajima*, 1995], both positive and negative correlations in scatterplots have been reported between satellite-observed COT and effective droplet radius. Difference among these COT$-r_e$ patterns can be attributed to difference in local aerosol concentrations. *Suzuki et al.* [2006] succeeded in reproducing similar COT$-r_e$ patterns in separate cloud simulations based on a two-dimensional nonhydrostatic bin cloud model for the conditions of the First ISCCP Regional Experiment (FIRE) and Atlantic Stratocumulus Transition Experiment (ASTEX) regions. The simulated COT$-r_e$ pattern for pristine conditions included a large proportion of negative correlation and a small fraction of positive correlation, while the pattern for polluted conditions exhibited an almost entirely positive correlation [*Suzuki et al.*, 2006, Figure 4].

[38] Figure 11 shows COT$-r_e$ scatter diagrams for cloud with top temperature higher than 265.15 K for the case shown in Figure 6 (2 April). Separate scatter diagrams are shown for the northern and southern parts for both the simulated and Terra/MODIS-derived variables, similar to Figure 10. In reference to the COT$-r_e$ patterns reported by *Suzuki et al.* [2006], the patterns in Figures 11c and 11d appear to be a combination of the pristine and polluted patterns. The present cloud microphysics therefore appears to differ from those in effect in the FIRE and ASTEX regions. It is worth noting that the COT$-r_e$ pattern in Figure 11c has a larger proportion of the pristine pattern than that in Figure 11d, indicating that the northern region may be more pristine than the southern region. This feature is consistent with the differences in simulated CN conditions between the northern and southern areas of the analysis domain (e.g., Figure 8).

Figure 10. Simulated and satellite-derived $T-r_e$ relationships between cloud top temperature (K) and effective droplet radius near the cloud top (μm) at 0300 UTC on 2 April 2003. Solid and dotted lines denote simulated and satellite-derived profiles, and black and gray lines denote profiles for the northern and southern parts of the analysis domain. (a) Standard run. (b) Uniform CN run. (c) Doubled CN run.

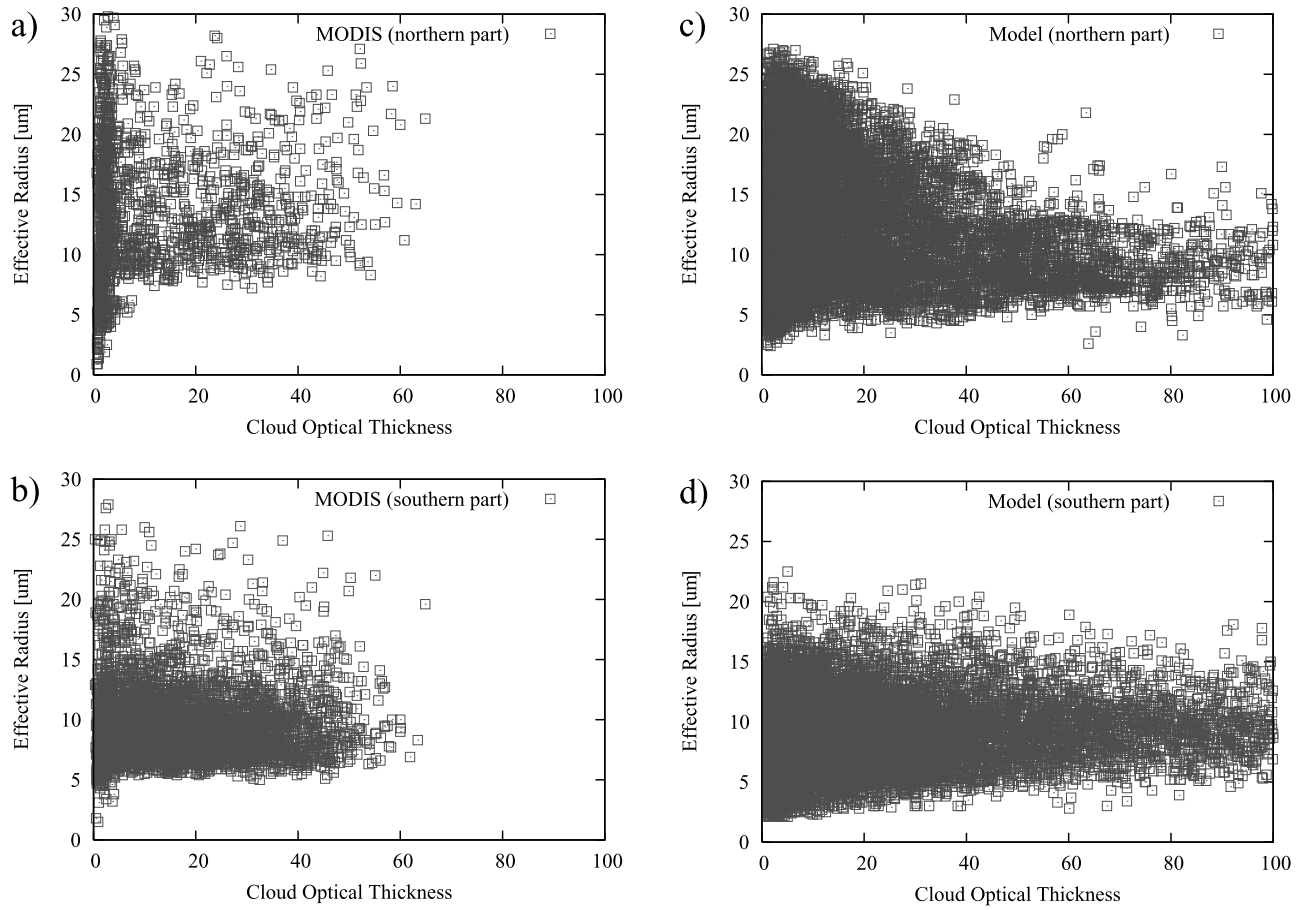

Figure 11. Simulated and satellite-derived COT-r_e scatter diagrams between cloud optical thickness and effective droplet radius near the cloud top (μm) at 0300 UTC on 2 April 2003. (a and b) Satellite-derived plots and (c and d) simulated plots for the north (Figures 11a and 11c) and south (Figures 11b and 11d).

[39] Quantitative estimation of these differences in the microphysical structures of cloud can be derived through a simple formulation of the relationship among observables assuming nonadiabatic cloud formation as proposed by *Szczodrak et al.* [2001, Appendix A]:

$$N_{sat} = \left(\frac{5C_w}{4\pi^2 Q_{ext}\rho_w}\right)^{1/2} \tau^{1/2} r_e^{-5/2} \approx kN_c/\sqrt{\beta}, \qquad (3)$$

where N_{sat} is the CDNC considering the departure of the liquid water content from the adiabatic value, C_w is the moist adiabatic condensation coefficient [*Brenguier et al.*, 2000], ρ_w is water density, τ is the cloud optical thickness, k is the ratio between the mean volume radius and the effective radius, N_c is the (total) CDNC, and β is a parameter representing the departure of the liquid water content profile from adiabatic. In the present model, C_w is set at 2.0×10^{-3} g m^{-3} m^{-1}.

[40] The simulated N_{sat} in the northern (pristine) and southern (polluted) areas are 27.2–336.4 cm^{-3} (average, 95.6 cm^{-3}) and 88.0–662.7 cm^{-3} (average, 241.5 cm^{-3}), corresponding to an average north/south ratio of 0.40. By comparison, the horizontally averaged CCN number concentrations at SS = 0.3% are 1.65×10^8 cm^{-2} in the north and 4.16×10^8 cm^{-2} in the south in the noncloud simulation run (Figure 3), also corresponding to a north/south ratio of 0.40. The variation in N_{sat} is thus consistent with the variation in CCN concentration. Both Terra/MODIS-derived COT–r_e patterns (Figures 11a and 11b) have a small proportion of the polluted pattern and a larger proportion of the pristine pattern, also indicating some dissimilarity in cloud microphysics from those in effect in the FIRE and ASTEX regions [*Suzuki et al.*, 2006, Figure 1]. In contrast, the satellite-derived COT–r_e pattern over the southern region (Figure 11b) has a larger proportion of the polluted pattern, with a concentration of small effective radius compared to that in Figure 11a. The N_{sat} values calculated from Terra/MODIS data are 16.4–175.7 cm^{-3} (average, 53.7 cm^{-3}) for the north and 71.7–373.5 cm^{-3} (average, 163.7 cm^{-3}) for the south. The spatial variation in the satellite-based values is thus in agreement with the simulations, although the simulation results in an overestimation of N_{sat}.

[41] The discrepancy between the present results and the COT–r_e patterns of *Suzuki et al.* [2006] is considered to be attributable to the less pronounced spatial variation of CN concentration in the present case compared to that between the FIRE and ASTEX regions in *Nakajima and Nakajima* [1995] and *Suzuki et al.* [2006]. Hence, the conditions in the present case appear to be a combination of the two extreme cases of these previous studies. The overestimation of

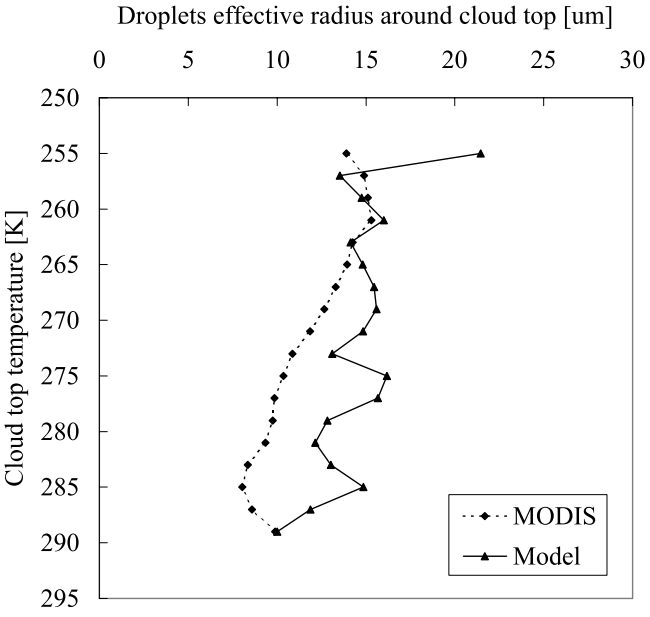

Figure 12. Simulated and satellite-derived T-r_e relationships between cloud top temperature (K) and effective droplet radius near the cloud top (μm) for the standard run at 0300 UTC on 8 April 2003. Solid and dotted lines denote simulated and satellite-derived profiles for the eastern part of the analysis domain.

simulated N_{sat} causes a larger spatial variation in cloud microphysical properties compared to the observations, resulting in a larger proportion of the polluted pattern in the present simulations and a weaker pristine pattern in the southern area (Figure 11d). The simulated field thus appears more polluted than the reality indicated by satellite observations.

[42] Figures 12 and 13 show the corresponding $T-r_e$ relations and COT$-r_e$ scatter diagrams for 8 April. The results are only shown for the eastern part (longitudes larger than 128°E) because the simulation could not accurately reproduce the thin cloud in the west. The plotted variables belong mostly to cloud associated with the cold front and the low-pressure system. The maximum radii of the simulated and observed $T-r_e$ relations in Figure 12 are in agreement. The simulated effective droplet radius remains relatively constant at close to 15 μm, while the satellite-derived effective radius increases in all layers with decreasing cloud top temperature to a maximum of $\sim$15 μm. The small effective radius observed in the lower layers is due to the optically very thin cloud (see Figure 7e), which has an effective radius of less than 9 μm (see Figure 7d) and covers a wide area of the analysis domain. As the simulation is unable to resolve this thin cloud (Figure 7a), the effective radius is overestimated. In Figure 13, the both the satellite-derived and simulated COT$-r_e$ scatter diagrams can be seen to be very similar to those for 2 April (Figure 11). The polluted pattern is dominant in the simulated diagram, where the effective radii are generally larger, while the satellite-derived diagram has a small proportion of the polluted pattern and a larger proportion of the pristine pattern. These patterns, both satellite-derived and simulated, appear characteristic of frontal-type cloud in this area and season.

3.5. Sensitivity Tests for CN Concentration

[43] Sensitivity test simulations were performed to examine the dependence of precipitation and the microphysics and dynamics of cloud on CN concentration. CN concentrations in all bins were set at 4.0 times and 0.1 times the values for the standard run (see section 2.3). The CCN number concentrations at supersaturation are proportional to the CN number concentrations if the predicted supersaturation in these runs is the same. Simulations using the bulk microphysics scheme for cloud originally implemented in the JMA-NHM were also performed. The bulk microphysical scheme is one-moment scheme accounting for two water and three ice types [*Ikawa and Saito*, 1991; *Yamada*, 2003].

[44] Figure 14 shows the distributions of simulated quantities for the fourfold 8 April run (similar to Figure 7). Figure 14 shows that elevated CN concentration causes a decrease in effective droplet radius due to an increase in the CDNC, and an increase in COT. The cloud top temperatures

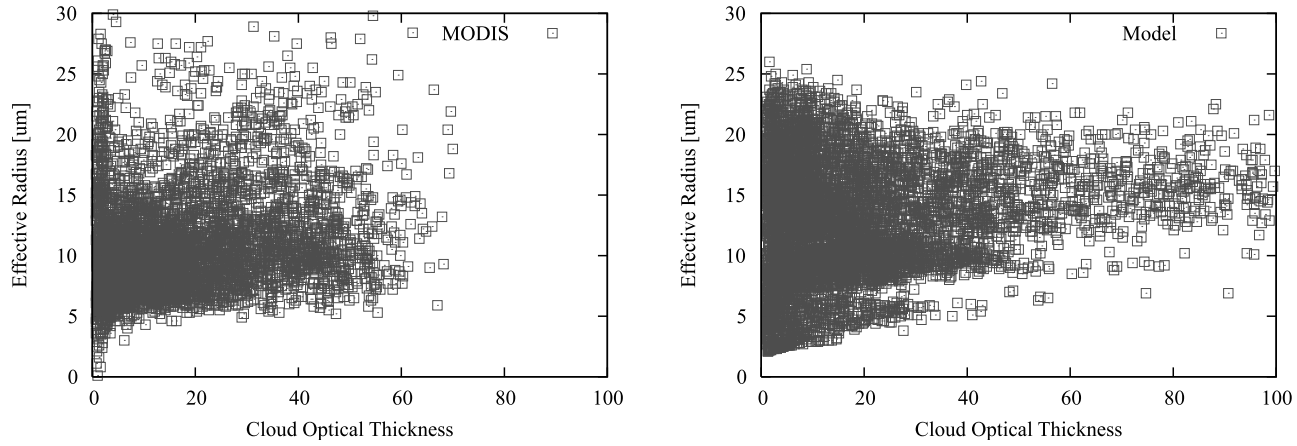

Figure 13. Simulated and satellite-derived COT-r_e scatter diagrams between cloud optical thickness and effective droplet radius near the cloud top (μm) for the eastern part of the analysis domain at 0300 UTC on 8 April 2003.

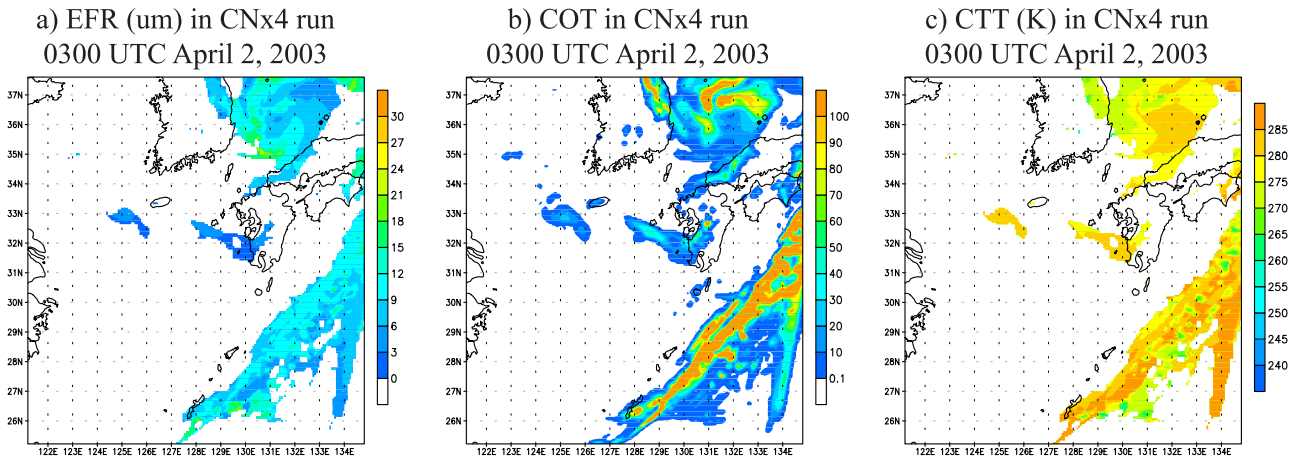

Figure 14. Simulated horizontal distributions of (a) effective droplet radius (μm) near the cloud top, (b) COT, and (c) cloud top temperature (K) for the fourfold CN run at 0300 UTC on 8 April 2003.

(heights), however, are largely invariant with respect to CN concentration, regardless of temperature.

[45] Figures 15 and 16 show the horizontal distributions of simulated LWP at 0300 UTC and the 1 h precipitation amounts from 0200 UTC to 0300 UTC on 2 and 8 April. Figures 15 and 16 also show the horizontal distributions of Terra/MODIS-derived LWP and 1 h precipitation reported by the JMA Radar-Automated Meteorological Data Acquisition System (AMeDAS) for the same times. Figure 17 shows the normalized frequency analysis of LWP and 1 h precipitation at the model grid points in the Radar-AMeDAS analysis region for the fourfold runs on 2 and 8 April. Despite the elevation of CN concentration, the areas of cloud and precipitation, including heavy precipitation (>5 mm/h) are essentially the same on 2 April as in the standard run (see Figures 15a–15d). On 8 April, the areas of cloud and precipitation are also similar to the standard run, although the area of heavy precipitation is reduced under the higher CN concentration scenario (Figures 16b and 16d). These results are interpreted below through comparison with the results of prior studies.

[46] Simulations of individual deep convective clouds within a sheared flow have revealed that the cloud top height is unaffected by the choice of high or low CN concentration [*Khain et al.*, 2005, Figure 5]. The low sensitivity of cloud top height to aerosols can be explained by three main mechanisms: the inhibition of cloud penetration by the existence of a stable layer in the upper atmosphere, counterbalance in buoyancy due to increases in both latent heat release and mass loading at elevated CN concentrations, and destruction of the upright structure of upper cloud by wind shear, which causes spreading of cloud and an increase in latent heat under the high CN condition to prevent an increase in cloud top height. In the presence of the wind shear, cloud under the high CN condition produce similar or smaller accumulated rain amounts depending on the air humidity. *Khain et al.* [2005, Figures 7, 8 and 10] analyzed the vertical profiles of latent heat balance. Cloud under the high CN condition generates larger latent heating by condensation, freezing, and deposition than cloud under the low CN condition, and larger cooling occurs at high CN concentration because of evaporation and sublimation in the upper layer of cloud. The effects of aerosols on precipitation at the surface are determined by the sign of the difference between the increase in condensate generation and condensate loss. Figure 18 shows vertical profiles of horizontally averaged latent heat budget (heating/cooling) due to condensation, deposition, evaporation, sublimation, freezing, and melting calculated for the present CN sensitivity tests. The conditions during the spring season over the East China Sea region are characterized by significant wind shear associated with the prevailing westerlies. In agreement with the findings of *Khain et al.* [2005, 2008], latent heating increases with CN concentration because of the enhanced production of condensate mass by diffusion growth. Cooling also increases with CN concentration.

[47] Net heating is maximal in the one-tenth run and minimal in the fourfold run, indicating that the average precipitation in the standard run is larger than that in the fourfold run. The altitudes at which heating/cooling become zero are invariant with respect to the CN condition, producing similar top heights. The environmental conditions in the target area thus lead to a decrease in precipitation under elevated CN concentration scenarios. Note that a decrease in precipitation occurs only in the high-precipitation area. The increase in evaporation and sublimation appears to be relatively small and to be offset by an increase in condensation and deposition when the cloud top is at an intermediate level. Such compensation may be the reason for the low sensitivity of surface precipitation to variations in CN concentration, and the balance between condensation and evaporation may be related to the environment conditions and cloud types [*Khain et al.*, 2008].

[48] CN has a pronounced influence on cloud microphysics and optical properties, yet has only a relatively small effect on precipitation. Figure 19 shows a time series of the ratios of horizontally averaged variables (instantaneous LWP, vertical integral of net water vapor convergence per hour, and 1 h precipitation) over the entire computational area with respect to CN concentration. Figure 19 clearly shows that the CN concentration has a marked effect on the LWP, with the difference in LWP increasing soon after the initial time and thereafter becoming relatively constant. No appreciable difference is apparent in water vapor converted

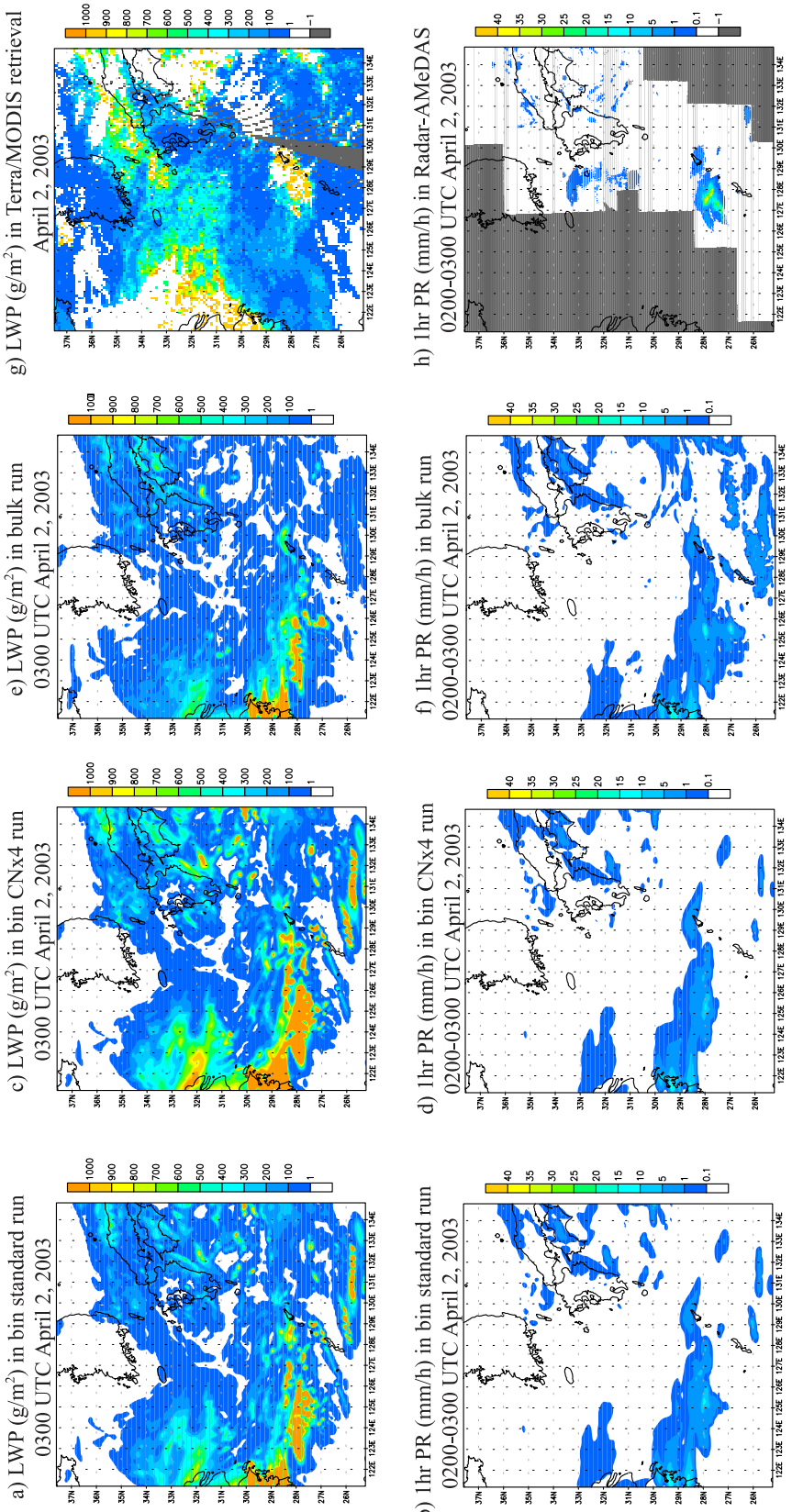

Figure 15. (a–f) Simulated and (g and h) satellite-derived horizontal distributions of LWP (g/m^2) at 0300 UTC on 2 April (Figures 15a, 15c, 15e, and 15g) and 1 h precipitation (mm/h) from 0200 UTC to 0300 UTC on 2 April (Figures 15b, 15d, 15f, and 15h) for the standard run (Figures 15a and 15b), fourfold CN run (Figures 15c and 15d), and bulk run (Figures 15e and 15d). Terra/MODIS-derived LWP and Radar-AMeDAS precipitation data are shown.

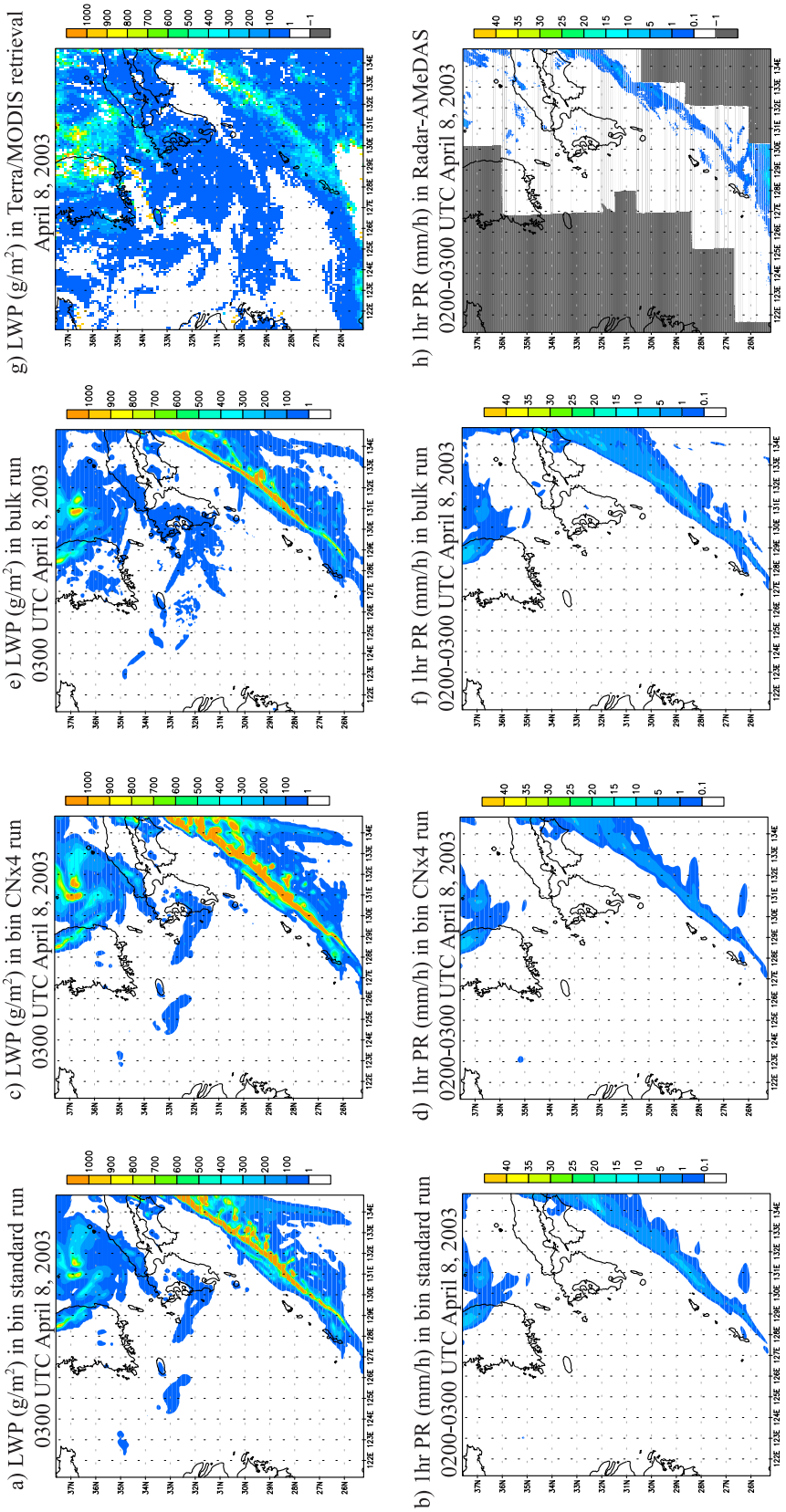

Figure 16. (a–f) Simulated and (g and h) satellite-derived horizontal distributions of LWP (g/m^2) at 0300 UTC on 8 April (Figures 16a, 16c, 16e, and 16g) and 1 h precipitation (mm/h) from 0200 UTC to 0300 UTC on 8 April (Figures 16b, 16d, 16f, and 16h) for the standard run (Figures 16a and 16b), fourfold CN run (Figures 16c and 16d), and bulk run (Figures 16e and 16d). Terra/MODIS-derived LWP and Radar-AMeDAS precipitation data are shown.

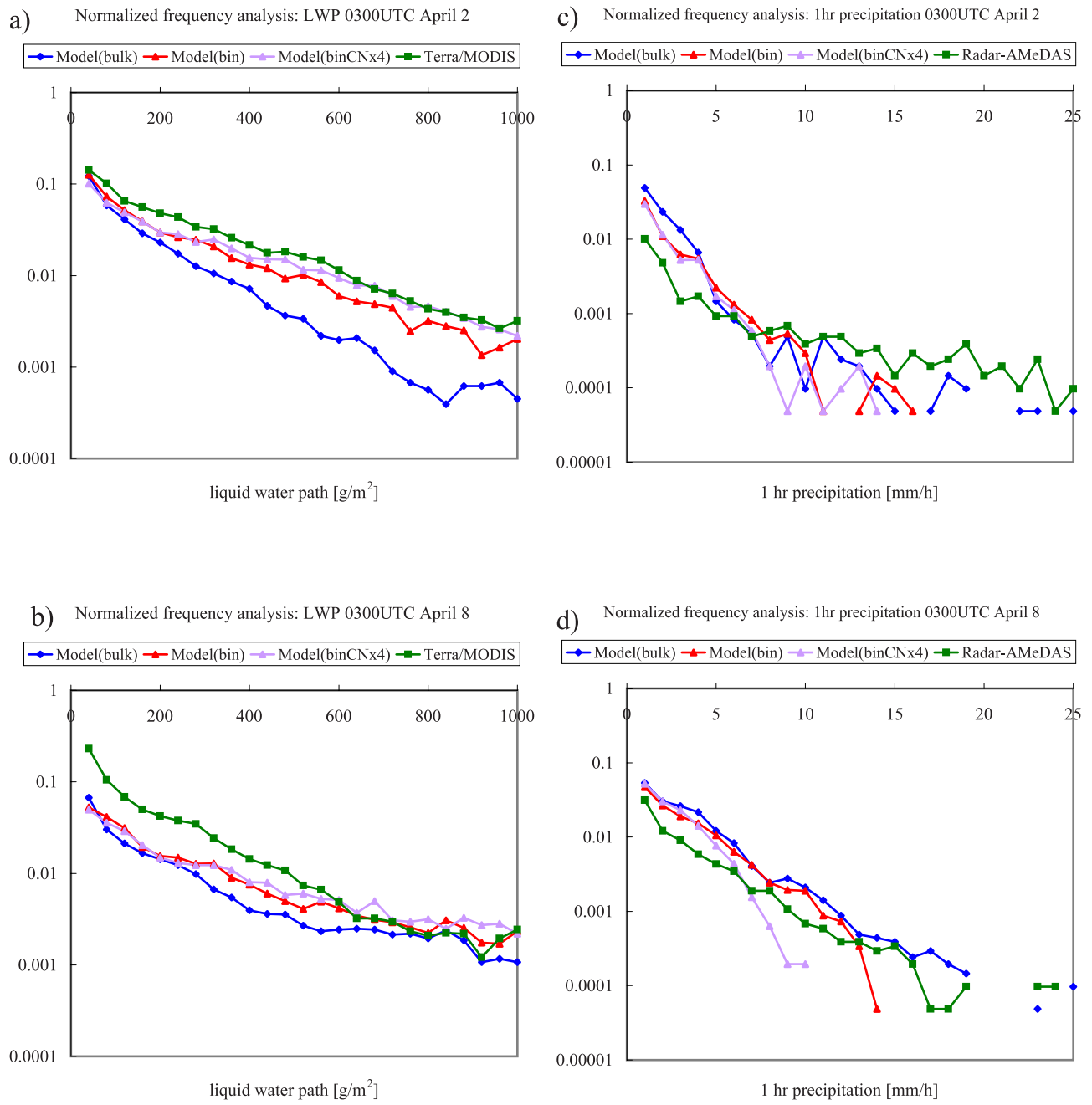

Figure 17. Normalized frequency plots of (a and b) LWP (g/m^2) at 0300 UTC on 2 April (Figure 17a) and 8 April (Figure 17b) and (c and d) 1 h precipitation (mm/h) from 0200 UTC to 0300 UTC on 2 April (Figure 17c) and 8 April (Figure 17d) for the model grid in the Radar-AMeDAS analysis region. Green denotes Terra/MODIS retrieval (Figure 17a) or Radar-AMeDAS analysis (Figure 17b), and blue, red, and violet denote simulation results for the bulk, standard, and fourfold CN runs, respectively.

to cloud water, which is apparently dependent on dynamics such as updraft velocity and moisture supply rather than cloud microphysics. A difference in precipitation can be seen a few hours into the simulation. Under conditions of elevated CN concentration, precipitation is delayed, causing a decrease in precipitation in the spin-up stage. The difference in precipitation after the initial stage, however, remains small (see Figure 16). The gain in LWP by water vapor convergence maintains balance with the loss due to precipitation if the precipitating cloud neither develops nor declines.

[49] It is worth stressing that the precipitation response to aerosols is dependent on the environmental conditions. *Lynn et al.* [2005b] conducted a nested grid simulation with a horizontal grid interval of 3 km in an attempt to resolve a squall line composed of organized convective cloud over Florida on 27 July 1991. The results were compared to similar simulations based on bulk cloud schemes. Results

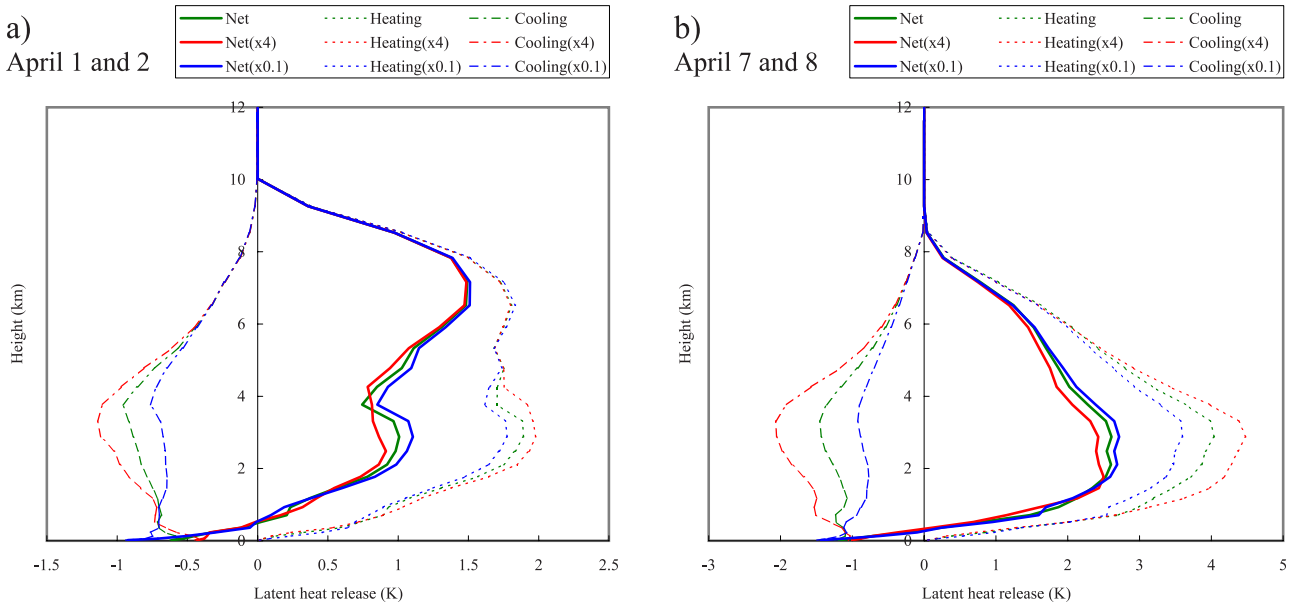

Figure 18. Vertical distributions of horizontally averaged latent heat budget (K) caused by cloud microphysical process for simulated cloud in each run. (a) 1800 UTC 1 April to 0300 UTC 2 April 2003. (b) 1800 UTC 7 April to 0300 UTC 8 April 2003. Green, red, and blue lines correspond to simulation results for the standard, fourfold CN, and one-tenth CN runs, respectively. Solid, dashed, and dash-dotted lines denote the net budget, heating, and cooling, respectively.

for both continental and maritime CN conditions were also presented using the same scheme with bin microphysics for cloud. The bin cloud model was found in the study of *Lynn et al.* [2005b] to reproduce the surface precipitation rate and radar reflectivity much more accurately than the bulk cloud model. An elevation of the CN concentration was also found to lead to an increase in precipitation rate in the zone of the squall line, although the accumulated precipitation over the entire computational area was largely similar for cases of both high and low CN concentration. The present CN sensitivity tests indicate that the 1 h precipitation amount is almost entirely insensitive to the CN concentration, and in fact decreases with increasing CN concentration in the intense precipitation area.

[50] The above two comparisons with prior studies suggest that precipitation changes with variation in the CN concentration in a manner dependent on several key factors of cloud formation: relative humidity (RH), wind shear, atmospheric instability, background forcing, and the timescale of formation. Relative humidity can influence the balance between condensation and evaporation and hence surface precipitation [*Khain et al.*, 2005, 2008]. In the present case, the environmental RH is not particularly high (~80% below 2 km on 2 April, ~70% below 2 km on 8 April), and is lower than that in the case considered by *Lynn et al.* [2005b] (90% in the boundary layer). Note that the thermodynamic conditions in the present case are also quite different from those of Florida in that the strong organized convection observed in Florida is absent in the present scenario.

[51] Figure 17 shows that the bin model simulates the LWP more accurately than the bulk model, and that the simulation of precipitation is improved by introducing the bin scheme. In Figure 15, the bin model can be seen to predict a small amount of precipitation over the sea in the southeast on 2 April, in agreement with that indicated by the Radar-AMeDAS analysis. Precipitation is strongly suppressed over this area at elevated CN concentration in the bin model, as shown in Figures 3, 8, and 9. In contrast, the bulk model simulation overestimates precipitation over this area. However, the areas of cloud and precipitation in both simulations are not substantially different. Both simulations produce common differences from the Radar-AMeDAS-analyzed precipitations. For example, the location of strong precipitation probably associated with local deep convection around 127.5°E, 27.5°N on 2 April (Figure 15h), and around 128.5°E, 25.5°N on 8 April (Figure 16h), is not reproduced accurately by the simulations. This disagreement can be attributed to general error in the model prediction of the dynamics fields. Models using explicit cloud microphysics are unable to generate cloud in zones of negative supersaturation. Note that the zones in which precipitation takes place is determined predominantly by large-scale forcing in these cases. It is thus reasonable to compare precipitation resolved by the bin and bulk simulations in zones in which the model predicts conditions suitable for cloud formation.

[52] The normalized frequency analysis in Figure 17 indicates that the total areas of 1 h precipitation in both simulations are larger than suggested by the Radar-AMeDAS analysis (see also Figure 16). *Lynn et al.* [2005b] also reported that the simulations overestimated the accumulated precipitation, attributing the error to the coarse resolution of the model (3 km). The effect of spatial resolution on the simulated variables was therefore examined here by performing additional simulations with horizontal grid intervals of 2 km (instead of 7 km in the control runs).

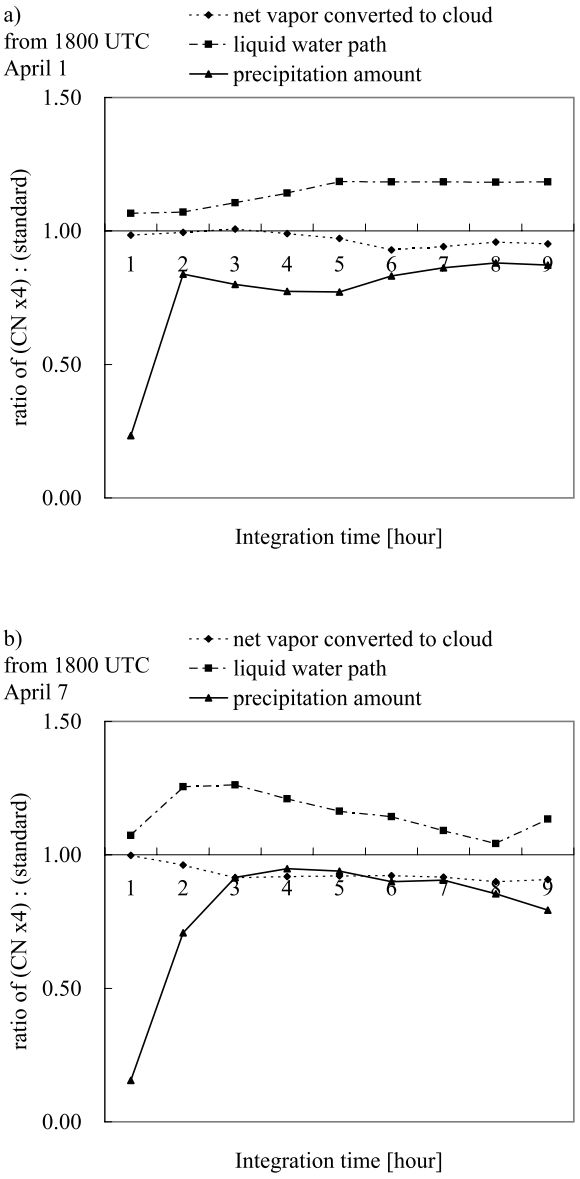

Figure 19. Time series of ratios of horizontally averaged LWP (dash-dotted), water vapor flux converted to cloud water (dashed), and surface precipitation flux (solid) for standard and fourfold CN runs. (a) 1800 UTC 1 April 2003. (b) 1800 UTC 7 April 2003.

The simulations treat only liquid phase microphysics and were computed for only 6 h in order to limit the computation requirements. Figure 20 shows the spatial distributions of variables in the simulations at resolutions of 2 km and 7 km. The results are generally in agreement, and the clouded areas and precipitation are similar. However, the 2 km simulation resolved small-scale clouds that are not represented or are smoothed out in the 7 km simulation. Figure 21 shows a normalized frequency analysis of the variables. The distributions of normalized frequencies are generally in agreement except for an increase in the frequency of heavy precipitation in the 2 km simulation. Heavy precipitation is likely to occur as a result of cloud development on small horizontal scales with large updraft velocity, which can only be reproduced by modeling at higher resolution. The frequency distributions of effective droplet radius is shifted slightly to larger sizes in the 2 km simulation, attributable to the ability of cloud in high-resolution simulation to hold larger particles under the influence of higher updraft velocity.

[53] The discussion above shows that while the standard simulation with 7 km resolution is unable to resolve small-scale cloud structures, such simulations remain very effective for reproducing large-area averages of cloud variables in the present cases. At horizontal resolutions of the order of kilometers, the concluding remarks in the former sections remain unchanged, because these analyses pertain to the characteristics of cloud variables averaged over large areas of the simulation domain rather than for specific clouds. The satellite data to which the results were compared are provided at a maximum resolution of 1 km. Prior studies using nonhydrostatic models with bulk microphysics for cloud [e.g., *Pauluis and Garner*, 2006] also showed that simulations with coarse horizontal resolution (e.g., 7 km) have the ability to reproduce cloud statistics with good accuracy. Nevertheless, the overestimation of the precipitation area remains to be solved, and will be addressed in future work in consideration of other causes such as uncertainties in the initial/boundary conditions, errors in satellite-derived fields, and surface precipitation measurements, in addition to problems with modeling. The progression to finer spatial resolution given advancements in computational resources will also be pursued in future work.

4. Summary and Conclusions

[54] In this study, a nonhydrostatic model including detailed cloud microphysics in a bin scheme was developed and applied to the analysis of aerosol effects on cloud microphysical properties. The bin model was coupled with a global-scale aerosol transport model for the first time by performing a nested grid simulation with inhomogeneous initial fields and temporally varying lateral boundary conditions also with respect to CN concentration. The initial and lateral boundary conditions were calculated using an interpolated field of aerosol concentrations generated by a SPRINTARS simulation. This off-line coupling makes it possible to calculate detailed microphysical variables such as the droplet size distribution, effective radius, LWP, COT, and precipitation over larger areas, considering the influence of aerosols.

[55] The simulated results were compared with data obtained by Terra/MODIS observations and Radar-AMeDAS precipitation analysis. The comparison showed that the combination of the bin microphysics scheme with the CN nesting procedure reproduces the main features of the spatial distribution of cloudiness and the microphysical properties of cloud indicated by satellite data. T–r_e relations calculated using this model were compared to those calculated from satellite-derived variables, and it was shown that the satellite-derived spatial variations in the T–r_e relations can be attributed to variations in CN concentration. The simulated and satellite-derived T–r_e relations exhibit similar tendencies in response to changes in CN concentration, in agreement with the changes indicated in previous studies based on other satellite-derived data [e.g., *Rosenfeld and Lensky*, 1998; *Rosenfeld*, 2000]. Sensitivity simulations

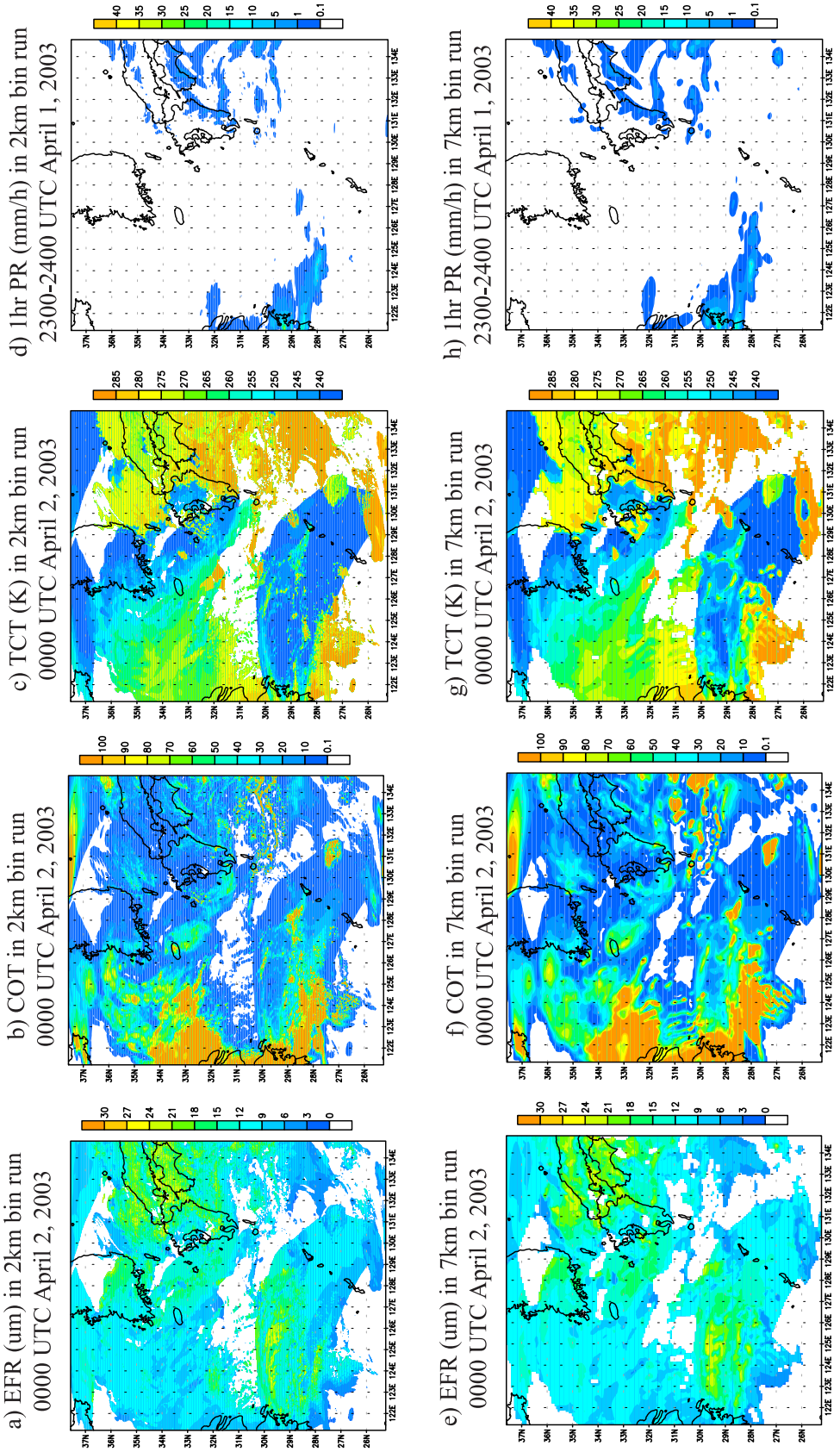

Figure 20. Simulated horizontal distributions for horizontal grid intervals of (a–d) 2 km (liquid phase microphysics only) and (e–h) 7 km for effective droplet radius (μm) near the cloud top (Figures 20a and 20e), COT (Figures 20b and 20f), and cloud top temperature (K) at 0000 UTC on 2 April (Figures 20c and 20g) and 1 h precipitation (mm/h) from 2300 UTC 1 April to 0000 UTC 2 April 2003 (Figures 20d and 20h). (i–p) Corresponding distributions for 8 April.

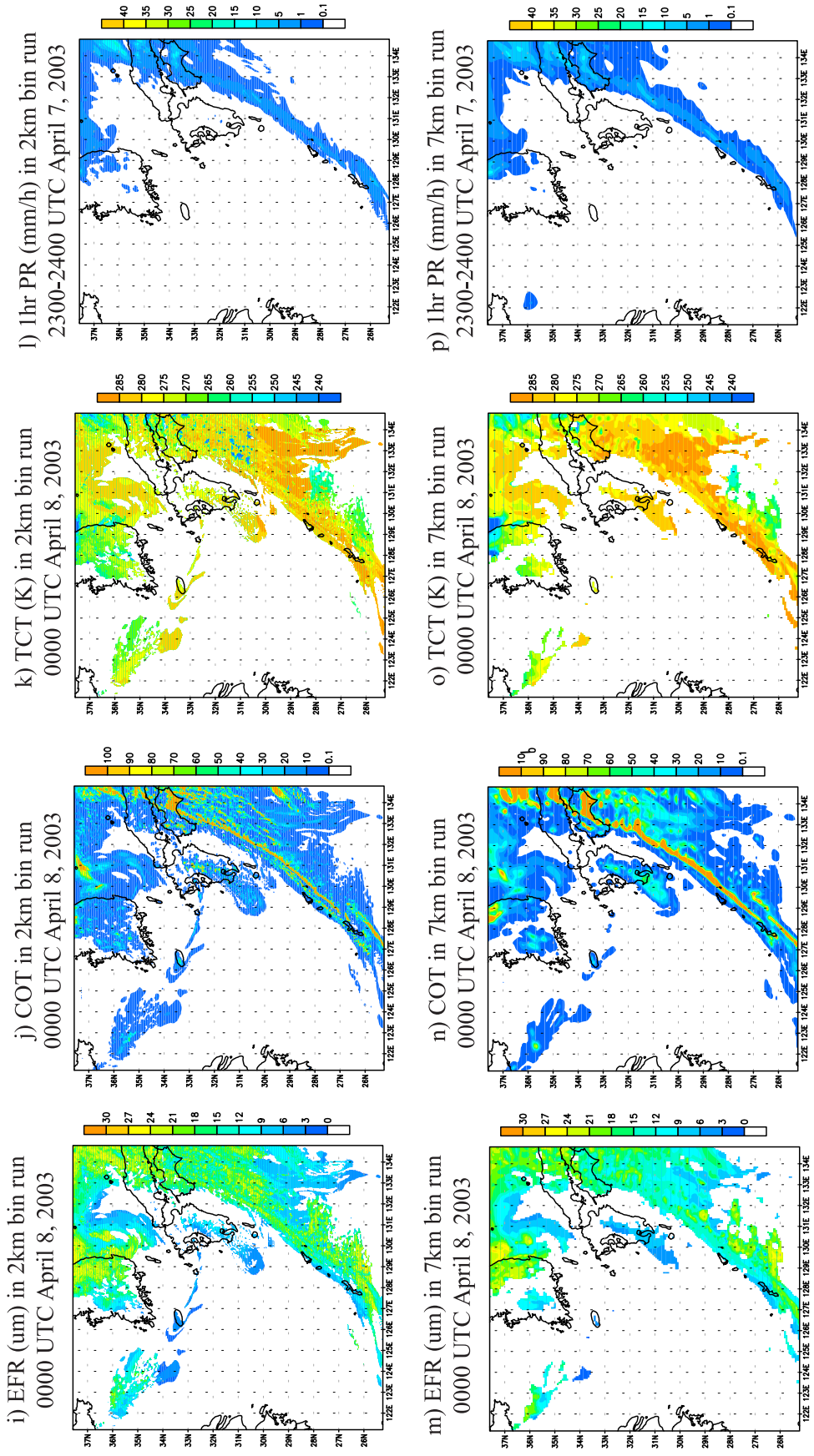

Figure 20. (continued)

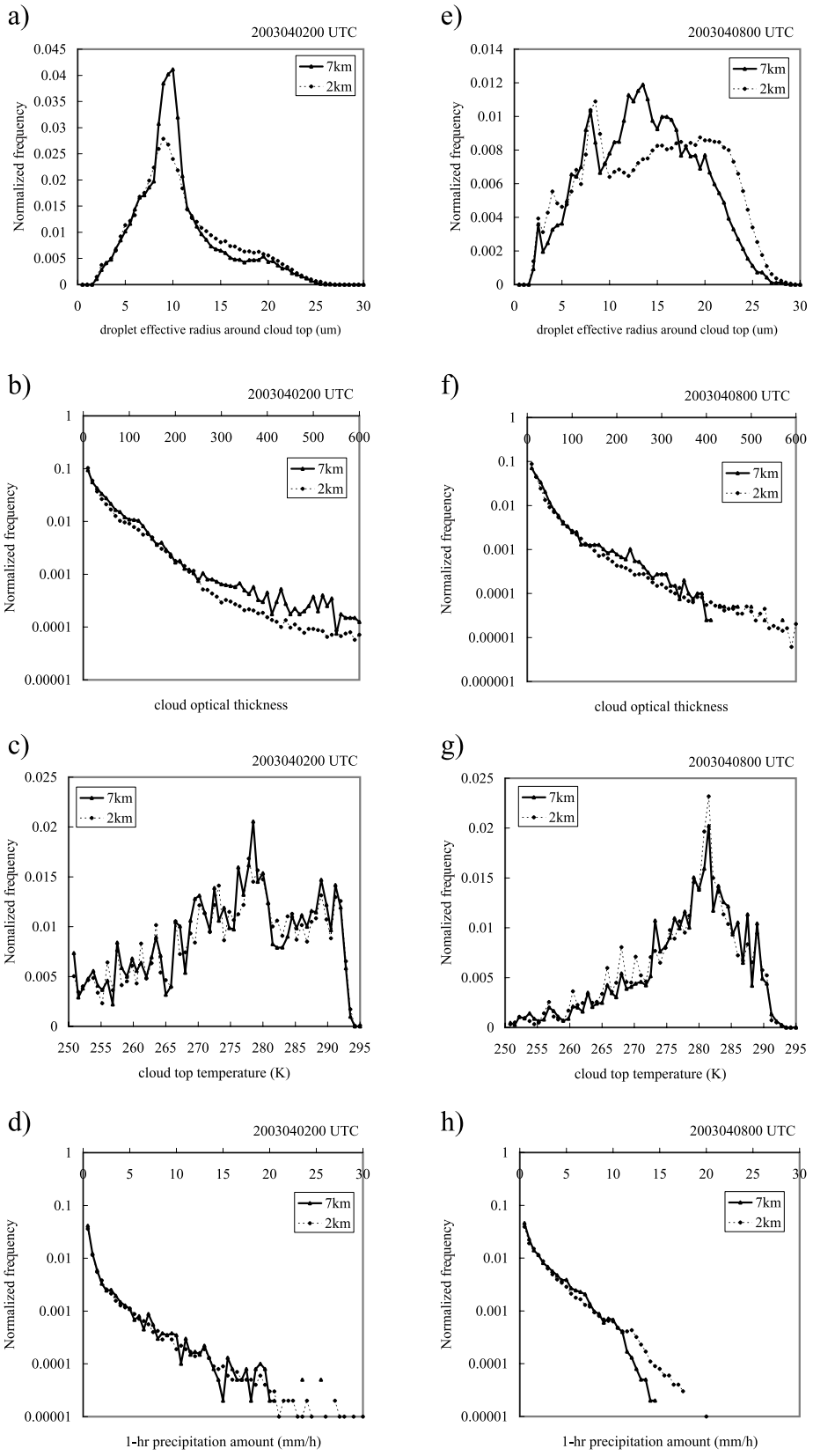

Figure 21. Normalized frequency plots of (a) effective droplet radius (μm) near the cloud top, (b) COT, (c) cloud top temperature (K) at 0000 UTC on 2 April, and (d) 1 h precipitation (mm/h) from 2300 UTC on 1 April to 0000 UTC on 2 April 2003. (e–h) Corresponding plots for 8 April. Solid lines and triangles denote simulations at a horizontal grid interval of 7 km, and dotted lines and solid circles denote 2 km resolution.

confirmed that the differences between simulated $T-r_e$ relations for the northern and southern parts of the analysis domain are caused mainly by differences in the average CN concentrations produced by the CN nesting procedure. Thus, it was found that the CN nesting procedure is effective for applying an inhomogeneous condition of CN concentration to the nested grid simulations, resulting in the reproduction of realistic cloud microphysical properties.

[56] COT$-r_e$ scatter diagrams were also presented for both simulated and satellite-derived variables. The present patterns were found to be a combination of the pristine and polluted patterns identified in previous studies for the FIRE and ASTEX regions [*Han et al.*, 1994; *Nakajima and Nakajima*, 1995; *Suzuki et al.*, 2006], without distinct positive or negative correlations. Such a combined pattern is probably obtained because of the relatively small difference in CN concentrations compared with that between the FIRE and ASTEX regions. The difference in environment, such as the higher sea surface temperatures of the spring East China Sea in the present cases, would also have given rise to different atmospheric instabilities. The role of CN concentration in cloud microphysics was therefore not as significant for the FIRE and ASTEX regions as found for the cases examined in the present study.

[57] The two main problems encountered in the present simulations were some inaccuracy in reproducing effective droplet radii, and overestimation of the cloud droplet number concentration. These inaccuracies are considered to be due not only to the coarse horizontal resolution but also to the error in forecasting dynamical fields.

[58] Sensitivity simulations revealed that the simulated variables were sensitive to the CN concentration. Precipitation decreased with increasing CN concentration, yet by no more than 10–15% under a fourfold increase in CN concentration. An analysis of the latent heat budget indicated that the increase in condensate production at elevated CN concentration is largely compensated for by an increase in precipitation loss due to increased sublimation and evaporation. Note that the meteorological conditions of the present nested grid simulations are typical of the spring season over the East China Sea region. The results of the present simulations are consistent with the results of *Khain et al.* [2005, 2008] and *Lynn et al.* [2005b], who showed that the precipitation response to aerosols is dependent on environmental conditions such as relative humidity, wind shear, synoptic-scale background forcing, and timescale of cloud formation. Further nested grid simulations and analyses using the bin microphysical scheme are required in order to understand how cloud dynamics and precipitation are controlled by environmental conditions.

[59] Using the proposed model with spectral bin microphysics, it is possible to calculate the size distribution and cloud microphysical parameters such as effective radius and radar reflectivity, which can be measured by satellite and radar. The precipitation predicted using the bin microphysical scheme does not differ substantially from that obtained using the bulk schemes, and for the present precipitation events caused by transitional synoptic-scale forcing, the difference in cloud microphysics did not appreciably affect the cloud dynamics or precipitation. Ensemble forecasting suggests that small differences in the initial condition and/or physical schemes can produce large variations in specific mesoscale disturbances [e.g., *Kalnay*, 2003, chapter 6]. Simulations using the present scheme should therefore be conducted also for such conditions.

[60] Knowledge of the characteristic dependencies of aerosol and cloud fields on the dynamics and cloud physics can be used to evaluate what type of model is suitable and most advantageous for each simulation region and each variable. The bin microphysical scheme can calculate the dynamics and microphysics of cloud, and precipitation including the aerosol effect, more directly and accurately than other approaches, albeit at greater computational cost. The bin model simulation conducted in the present study using the CN nesting procedure resulted in a more accurate prediction of suppressed precipitation under polluted conditions, whereas bulk simulations tended to overestimate precipitation. On the other hand, there are also variables that do not depend strongly on the detailed size distributions of CN and cloud particles, at least under the specific conditions of the spring season over the east Asian region. In these cases, the bulk model affords relatively accurate precipitation with lower computational cost. Bulk models are thus suited to short-period numerical weather prediction for cloudiness and precipitation in cases that do not involve significant interaction with aerosols. At the same time, the bin model becomes particularly useful when cloud microphysics play an important role in determining cloud dynamics, such as in the study of feedback processes and climate projection simulations. The bin model is also advantageous for studies involving satellite data, since satellite observables can be calculated directly from the size distribution and other variables. The bin model may also prove useful in the improvement of satellite retrieval. New methods of mesoscale remote sensing, such as Doppler cloud radar and microwave radiometer, are also expected to provide useful data for coupling with the bin microphysical scheme, potentially providing information such as the size of hydrometeors.

Appendix A: Modeling of Cloud Microphysics

[61] The bin cloud microphysical scheme introduced in the present study is based on the module package in the Hebrew University Cloud Model (HUCM) [*Khain and Sednev*, 1995, 1996; *Khain et al.*, 2000]. This scheme treats droplet and ice crystal nucleation, condensation and deposition growth, evaporation, sublimation, droplet freezing (immersion freezing), melting, and coalescence growth for 7 types of hydrometeors (water droplets, ice crystals (plate, column, dendrite), snow, graupel, and hail). Graupel and hail are both characterized as rimmed particles, although with different bulk densities. The basic conservation equation for hydrometeors is given by

$$\frac{\partial f_{i,k}}{\partial t} + Adv.\left(f_{i,k}\right) - Drp.\left(f_{i,k}\right) = -\left[\frac{\partial f_{i,k}}{\partial t}\right]_{\text{micro}}, \qquad \text{(A1)}$$

where $f_{i,k}$ is the size distribution function of hydrometeors in a size bin category defined by the subscripts $i(= 1, \ldots 7)$ denoting the type of hydrometeor and $k(= 1, \ldots 33)$ denoting the bin size number. *Adv.* and *Drp.* represent

advection and gravitational sedimentation, and the term $[]_{micro}$ denotes the rate of change due to cloud microphysical processes.

[62] The nucleation of water droplets is calculated using the following theories. Supersaturation around a droplet containing a soluble part in equilibrium with its environment is described by the Köhler equation [e.g., *Rogers and Yau*, 1989], as given by

$$S_w = \frac{A}{r_w} - \frac{Br_{cn}^3}{r_w^3}, \tag{A2}$$

where

$$A \approx \frac{3.3 \times 10^{-5}}{T}(\mathrm{cm}) \text{ and } B \approx \frac{4.3v}{M_{cn}}\left(\frac{4\pi\rho_{cn}}{3}\right). \tag{A3}$$

Here, S_w is the supersaturation over water, r_w is the radius of the droplet, and r_{cn} is the radius of the CN. In equation (A3), T is temperature, v is the van't Hoff factor [e.g., *Low*, 1969], M_{cn} is the molecular weight of the component of CN, and ρ_{cn} is the density of CN. The chemical composition of CN is assumed to be ammonium sulfate ($(NH_4)_2SO_4$) and to be uniform. In equation (A2), the maximum supersaturation for any droplet radius is determined using the condition, $dS_w/dr_w = 0$, with maximum defined by

$$S_{crit(w)} = \frac{2A}{3r_{crit(w)}}, \tag{A4}$$

where

$$r_{crit(w)} = \sqrt{\frac{3Br_{cn}^3}{A}}.$$

The term $r_{crit(w)}$ denotes the droplet radius calculated by substituting $S_{crit(w)}$ for S_w in equation (A2). The critical radius of CCN, $r_{crit(ccn)}$, is calculated from $S_{crit(w)}$ by

$$r_{crit(CCN)} = \left(\frac{4}{27}\frac{A^3}{B}\frac{1}{S_{crit(w)}}\right)^{1/3}. \tag{A5}$$

All CN larger than the critical radius $r_{crit(ccn)}$ calculated by equation (A5) is assumed to be converted to cloud droplets.

[63] The nucleation of ice crystals is calculated using the parameterization suggested by *Meyers et al.* [1992]. This parameterization assumes ice crystals formed by heterogeneous nucleation and condensation followed by freezing [*Rogers and Yau*, 1989], as described by

$$N_d = 10^{-3}\exp(-0.639 + 12.96S_{ice})\left[\mathrm{m}^{-3}\right], \tag{A6}$$

where N_d is the number concentration of newly generated ice crystals, and S_{ice} is the supersaturation over ice. The type of generated ice crystal depends on the ambient temperature [*Takahashi et al.*, 1991].

[64] Condensation, deposition, evaporation, and sublimation are calculated using the scheme proposed by *Khain and Sednev* [1996]. The change in mass of hydrometeors due to these processes is given analytically by [e.g., *Rogers and Yau*, 1989]

$$\frac{dm_w}{dt} = \frac{4\pi r_w S_w}{F_w} \text{ and } \frac{dm_{ice}}{dt} = \frac{4\pi C_{ice} S_{ice}}{F_{ice}}, \tag{A7}$$

where

$$F_w = \frac{R_v T}{e_{s(w)} D_v} + \frac{L_w}{K_\alpha T}\left(\frac{L_w}{R_v T} - 1\right)$$
$$\text{and } F_{ice} = \frac{R_v T}{e_{s(ice)} D_v} + \frac{L_{ice}}{K_\alpha T}\left(\frac{L_{ice}}{R_v T} - 1\right). \tag{A8}$$

where m_w and m_{ice} are the masses of hydrometeors (water droplets or ice particles), C_{ice} is the shape factor of ice hydrometeors [*Khain and Sednev*, 1996], R_v is the gas constant of water vapor, $e_{s(w)}$ and $e_{s(ice)}$ are the saturation vapor pressures over water and ice, D_v is the diffusivity of water vapor, L_w and L_{ice} are the specific latent heats of vaporization over water and sublimation over ice, and $K\alpha$ is the thermal conductivity of air. In equation (A7), the effects of the solution and curvature are assumed to be negligible. Equation (A7) is replaced with a differential equation of supersaturation, considering the changes in water vapor and temperature due to these processes, as given by

$$\frac{dS_w}{dt} = -P_1 S_w - P_2 S_{ice} \text{ and } \frac{dS_{ice}}{dt} = -R_1 S_w - R_2 S_{ice}, \tag{A9}$$

where

$$P_1 = \frac{e}{e_{s(w)}}\left(\frac{1}{q(0.622+q)} + \frac{L_w^2}{C_p T^2 R_v}\right)\int_0^\infty \frac{4\pi r_w}{F_w} f_{i=w,k}\,dm,$$
$$P_2 = \frac{e}{e_{s(w)}}\left(\frac{1}{q(0.622+q)} + \frac{L_{ice}L_w}{C_p T^2 R_v}\right)\sum_{i=ice}\int_0^\infty \frac{4\pi C_{ice}}{F_{ice}} f_{i,k}\,dm,$$
$$R_1 = \frac{e}{e_{s(ice)}}\left(\frac{1}{q(0.622+q)} + \frac{L_{ice}L_w}{C_p T^2 R_v}\right)\int_0^\infty \frac{4\pi r_w}{F_w} f_{i=w,k}\,dm,$$
$$R_2 = \frac{e}{e_{s(ice)}}\left(\frac{1}{q(0.622+q)} + \frac{L_{ice}^2}{C_p T^2 R_v}\right)\sum_{i=ice}\int_0^\infty \frac{4\pi C_{ice}}{F_{ice}} f_{i,k}\,dm,$$

where e is the vapor pressure, q is the mixing ratio of water vapor, C_p is the specific heat of dry air at constant pressure, $f_{i=w,k}$ is the size distribution function of water droplets, and $\Sigma_{i=ice}$ denotes the sum for the 6 types of ice hydrometeors. In the actual computation, the numerical integration of equations (A7) and (A9) is performed with a time interval of Δt_m to calculate the evolution of the size distribution function $f_{i,k}$. $\Delta t_m = m_{min}F/4\pi rS$ is calculated from equation (A7), where m_{min} is the minimum mass in the hydrometeors bins. The numerical integration of equations (A7) and (A9) is repeated while the total of Δt_m is less than the time interval used for the integration of dynamics.

[65] Droplet freezing (immersion freezing) is calculated using two types of parameterizations, and the selection of parameterization is dependent on the ambient temperature. The parameterization by *Ovtchinnikov and Kogan* [2000] is

used when the temperature is higher than 235.15 K, for which the number concentration of activated immersion nuclei per unit volume of liquid water is given by

$$N_{\mathrm{im}} = N_{\mathrm{im0}}(0.1T)^{4.4}, \tag{A10}$$

where $N_{\mathrm{im}0}$ is the number concentration of all immersion nuclei per unit volume of liquid water. The type of ice particles generated by freezing is dependent on the size of frozen water droplets, where frozen water droplets with radii smaller than 200 μm are converted to plate-like ice crystals of corresponding mass, while larger frozen droplets are transformed to hail. The parameterization by *Bigg* [1953] is applied when the temperature is lower than 235.15 K, for which the freezing probability is assumed to be proportional to the droplet mass. The decrease in the size distribution function of water droplets is calculated by

$$\frac{1}{f_{i=\mathrm{w},k}}\frac{\partial f_{i=\mathrm{w},k}}{\partial t} = -10^{-4} m_{\mathrm{w}} \exp(-0.66T)\left[\mathrm{s}^{-1}\mathrm{g}^{-1}\right]. \tag{A11}$$

The type of ice particles generated is determined in the same manner as in the alternative parameterization.

[66] The melting of ice hydrometeors is calculated simply assuming all ice hydrometeors are converted to water droplets of corresponding mass when the ambient temperature exceeds 273.15 K.

[67] Coalescence growth is determined on the basis of a stochastic coalescence model [*Khain and Sednev*, 1995; *Pruppacher and Klett*, 1997], as expressed by

$$\begin{aligned}\frac{\partial f_i(m)}{\partial t} = &-\sum_{i'=1}^{i'=7}\int_0^{\infty} f_i(m)K_{i,i'}(m,m')f_{i'}(m')\mathrm{d}m' \\ &+\sum_{i''=1}^{i''=7}\sum_{i'=1}^{i'=i''}\delta(i;i',i'',T)\int_0^{m/2} f_{i''}(m-m') \\ &\cdot K_{i',i''}(m',m-m')f_{i'}(m')\mathrm{d}m',\end{aligned} \tag{A12}$$

$$\begin{aligned}K_{i,i'}(m,m') = &\pi\{r_i(m)+r_{i'}(m')\}^2|V_i(m)-V_{i'}(m')| \\ &\cdot E_{\mathrm{col};i,i'}(m,m')E_{\mathrm{coal};i,i'}(m,m'),\end{aligned} \tag{A13}$$

$$\delta(i;i',i'',T) = \begin{cases} 1, \text{ if type } i \text{ is generated using types } i' \text{ and } i'' \text{ under temperature } T \\ 0, \text{ otherwise} \end{cases}, \tag{A14}$$

where V is the terminal velocity of hydrometeors, E_{col} is the collision efficiency, and E_{coal} is the coalescence efficiency factor. The type of particles after coalescence is dependent on the type of the parent particles and the ambient temperature [*Khain and Sednev*, 1996, Table 2]. An accurate method of solving the stochastic coalescence equation (A12) [*Bott*, 1998] is employed. This method prevents artificial spectrum broadening by stochastic coalescence.

[68] Gravitational sedimentation is calculated using a box-Lagrangian raindrop scheme [*Kato*, 1995] instead of the Eulerian scheme in the original HUCM. The box-Lagrangian scheme was developed in the framework of the bulk microphysical scheme [*Ikawa and Saito*, 1991]. Thus, the rain terminal velocity V_{r} in the work by *Kato* [1995, equation 1] is assumed: $V_{\mathrm{r}} = Aq_{\mathrm{r}}n$, where q_{r} is the mixing ratio of rain and A and n are positive constants. The terminal velocity is substituted for each size bin of hydrometeors in coupling of the bin scheme to the box-Lagrangian scheme. The particles in each size bin of hydrometeors have different terminal velocities, dependent on the mass, type of hydrometeor, and the air density [*Khain and Sednev*, 1995, 1996]. This coupling leads to a more detailed calculation of gravitational sedimentation compared to the original coupling of the bulk scheme because particles of different sizes can fall separately and the calculation includes no uncertainties in A and n.

Appendix B: Modeling of Cloud Nuclei With Nesting Procedure

[69] The basic conservation equation for cloud nuclei is expressed as

$$\frac{\partial f_{\mathrm{cn},l}}{\partial t} + Adv.\left(f_{\mathrm{cn},l}\right) = -\left[\frac{\partial f_{\mathrm{cn},l}}{\partial t}\right]_{\mathrm{nucleation}} + Dif.\left(f_{\mathrm{cn},l}\right), \tag{B1}$$

where $f_{\mathrm{cn},l}$ is the size distribution function of CN in each size bin denoted by subscript l, and the term $[]_{\mathrm{nucleation}}$ denotes the rate of reduction due to activation (nucleation to droplets). The only source of CN is inflow from the lateral boundaries, and the sink is due to outflow at the lateral boundaries and consumption by nucleation. The terminal falling velocity of CN is neglected.

[70] An inhomogeneous initial field and temporally variable lateral boundary conditions with respect to CN concentration are applied by introducing a nesting procedure. The interpolation in the nesting procedure is applied to the distribution of aerosol concentration given by a global numerical simulation using the SPRINTARS [e.g., *Takemura et al.*, 2000], for five tropospheric aerosols (organic carbonaceous, black carbonaceous, soil dust, sulfate, and sea salt aerosols). Organic carbonaceous, sulfate, and sea salt aerosols among are assumed to be hygroscopic and hence be CN, which can serve as CCN. The concentrations of hygroscopic aerosols are given by the SPRINTARS run, and are then converted to a size distribution function of CN on a nested grid point. The conversion is performed using the concentration of each hygroscopic aerosol in the form of a bulk number concentration of dry particles. The bulk number concentration is then converted to a size distribution of CN in bins, assuming a size distribution that is dependent on the aerosol type [*Takemura et al.*, 2002]. The size distributions of organic carbonaceous and sulfate aerosols are assumed to have lognormal forms. The size distributions of CN converted from organic carbonaceous and sulfate aerosols number concentrations are given by

$$f_{cn(OC),l} = \frac{N_{OC}}{\sqrt{2\pi}\sigma_{OC}}\exp\left[-\frac{1}{2}\left\{\frac{\ln\left(B^{1/3}/B_{OC}^{1/3}\cdot r_{cn,l}/r_{OC}\right)}{\sigma_{OC}}\right\}^2\right], \tag{B2}$$

$$f_{cn(SU),l} = \frac{N_{SU}}{\sqrt{2\pi}\sigma_{SU}} \exp\left[-\frac{1}{2} \left\{ \frac{\ln\left(B^{1/3} / B_{SU}^{1/3} \cdot r_{cn,l} / r_{SU} \right)}{\sigma_{SU}} \right\}^2 \right], \tag{B3}$$

where OC and SU denote parameters for organic carbonaceous and sulfate aerosols, N is the bulk number concentration of aerosols given by the SPRINTARS run, r is the mode radius, and σ is the standard deviation of the size distribution. In the present study, the values of $r_{OC} = 0.1$ μm and $\sigma_{OC} = 1.8$ are adopted for organic carbonaceous aerosols, and $r_{SU} = 0.0695$ μm and $\sigma_{SU} = 2.03$ are employed for sulfate aerosols following *Takemura et al.* [2002, Table 4]. B_{SA} and B_{SU} correspond to B in equation (A3) except for the use of the van't Hoff factors, molecular weights, and the densities of organic carbonaceous and sulfate aerosols, respectively; these B_{SA} and B_{SU} were assumed to be equal to B using the parameters of ammonium sulfate in this study because the chemical components to determine these parameters are uncertain especially about organic carbonaceous aerosols. The size distribution of CN converted from the bulk number concentration of sea salt aerosols is given by

$$f_{\mathrm{cn},l} = 1.5 N_{\mathrm{SA}} K \left(\frac{B_{\mathrm{SA}}}{B} \frac{r_{\mathrm{SA}}}{r_{\mathrm{cn},l}^3} \right)^K, \tag{B4}$$

where N_{SA} is the bulk number concentration of sea salt aerosols, and B_{SA} corresponds to B in equation (A3) except for the use of the parameters of sea salt aerosol, and $r_{SA} = 0.1$ μm. The sum of equations (B2), (B3) and (B4) gives the size distribution of CN in nested grid simulations.

[71] The CN concentration in each bin is calculated using the same lateral boundary conditions as employed for potential temperature and the mixing ratio of water vapor. The lateral boundary conditions for these prognostic variables are as follows. In the Arakawa-C grid structure adopted for horizontal discretization, external and internal grid points are defined adjacent to the lateral boundary. The external nested value is defined by the temporal and spatial interpolation of a precalculated field of the outer model or reanalysis data on the external grid point. Temporal integration of the prognostic variable on the external grid point is then performed by [*Ikawa and Saito*, 1991]

$$f_{\mathrm{out}}^{\tau+1} = \beta f_{\mathrm{EXT}}^{\tau} + (1-\beta)\left(2f_{\mathrm{in}}^{\tau} - f_{\mathrm{in}-1}^{\tau-1}\right) \text{ at the outflow boundary}, \tag{B5}$$

$$f_{\mathrm{out}}^{\tau+1} = \beta f_{\mathrm{EXT}}^{\tau} + (1-\beta) f_{\mathrm{out}}^{\tau-1} \text{ at the inflow boundary}, \tag{B6}$$

where f_{out} and f_{in} are values on the external and inertial grid points adjacent to the lateral boundary, $f_{in\text{-}1}$ is the value on the grid point next to the internal grid point, f_{EXT} is the external nested value, β is a weighting parameter, and the index τ is the number of the time step level. Inflow and outflow are determined by the normal wind component at the lateral boundary.

[72] **Acknowledgments.** This research was supported by the Global Environment Research Fund B-4 of the Ministry of Environment, Japan, by project RR2002 and the Data Integration for Earth Observation project of the Ministry of Education, Sports, Science, Culture and Technology (MEXT) of Japan, and by the JAXA/ADEOS-II GLI project. One of the authors (A. K.) is supported by a grant from the Israel Science Foundation (140/07). The authors wish to gratefully acknowledge the developers of the JMA-NHM and HUCM, Takashi Nakajima of Tokai University for providing Terra/MODIS cloud retrieval data and RGB Images, and Yutaka Ishizaka of Nagoya University for providing aircraft observation data acquired in the APEX E-3 campaign. Nick Schutgens is also thanked for valuable discussion on improving the manuscript.

References

Adhikari, M., Y. Ishizaka, H. Minda, R. Kazaoka, J. B. Jensen, J. L. Gras, and T. Nakajima (2005), Vertical distribution of cloud condensation nuclei concentrations and their effect on microphysical properties of clouds over the sea near the southwest islands of Japan, *J. Geophys. Res.*, *110*, D10203, doi:10.1029/2004JD004758.

Albrecht, B. A. (1989), Aerosols, cloud microphysics, and fractional cloudiness, *Science*, *245*, 1227–1230, doi:10.1126/science.245.4923.1227.

Arnason, G., and R. S. Greenfield (1972), Micro- and macro-structures of numerically simulated convective cloud, *J. Atmos. Sci.*, *29*, 342–367, doi:10.1175/1520-0469(1972)029<0342:MAMSON>2.0.CO;2.

Bigg, E. K. (1953), The formation of atmospheric ice crystals by the freezing of droplets, *Q. J. R. Meteorol. Soc.*, *79*, 510–519, doi:10.1002/qj.49707934207.

Bott, A. (1998), A flux method for the numerical solution of the stochastic collection equation, *J. Atmos. Sci.*, *55*, 2284–2293, doi:10.1175/1520-0469(1998)055<2284:AFMFTN>2.0.CO;2.

Brenguier, J.-L., H. Pawlowska, L. Schüller, R. Preusker, J. Fischer, and Y. Fouquart (2000), Radiative properties of boundary layer clouds: Droplet effective radius versus number concentration, *J. Atmos. Sci.*, *57*, 803–821, doi:10.1175/1520-0469(2000)057<0803:RPOBLC>2.0.CO;2.

Chen, J. P., and D. Lamb (1994), Simulation of cloud microphysical and chemical processes using a multicomponent framework. Part I: Description of the microphysical model, *J. Atmos. Sci.*, *51*, 2613–2630, doi:10.1175/1520-0469(1994)051<2613:SOCMAC>2.0.CO;2.

Clarke, A. D., and V. N. Kapustin (2002), A Pacific aerosol survey. Part I: A decade of data on particle production, transport, evolution, and mixing in the troposphere, *J. Atmos. Sci.*, *59*, 363–382, doi:10.1175/1520-0469(2002)059<0363:APASPI>2.0.CO;2.

Dudhia, J. (1993), A nonhydrostatic version of the Penn State-NCAR mesoscale model: Validation test and simulation of an Atlantic cyclone and cold front, *Mon. Weather Rev.*, *121*, 1493–1513, doi:10.1175/1520-0493(1993)121<1493:ANVOTP>2.0.CO;2.

Feingold, G., and S. M. Kreidenweis (2002), Cloud processing of aerosol as modeled by a large eddy simulation with coupled microphysics and aqueous chemistry, *J. Geophys. Res.*, *107*(D23), 4687, doi:10.1029/2002JD002054.

Gal-Chen, T., and R. C. J. Somerville (1975), On the use of a coordinate transform for the solution of the Navier-Stokes equation, *J. Comput. Phys.*, *17*, 209–228, doi:10.1016/0021-9991(75)90037-6.

Grell, G., J. Dudhia, and D. R. Stauffer (1994), A description of the fifth generation Penn State/NCAR Mesoscale Model (MM5), *NCAR Tech. Note, NCAR/TN-398+STR*, 121 pp., Natl. Cent. for Atmos. Res., Boulder, Colo.

Han, Q., W. B. Rossow, and A. A. Lacis (1994), Near-global survey of effective droplet radii in liquid water clouds using ISCCP data, *J. Clim.*, *7*, 465–497, doi:10.1175/1520-0442(1994)007<0465:NGSOED>2.0.CO;2.

Ikawa, M., and K. Saito (1991), Description of a non-hydrostatic model developed at the Forecast Research Department of the MRI, *Tech. Rep. MRI*, *28*, 238 pp., Meteorol. Res. Inst., Tsukuba, Japan.

Intergovernmental Panel on Climate Change (2007), *Climate Change 2007: The Physical Science Basis-Contribution of Working Group I to the Fourth Assessment Report of the Intergovernmental Panel on Climate Change*, edited by S. Solomon et al., Cambridge Univ. Press, Cambridge, U. K.

Ishizaka, Y. (2004), Report of aircraft observations during APEX campaigns (in Japanese), report, 82 pp., Hydrospheric Atmos. Res. Cent., Nagoya Univ., Nagoya, Japan, 20 Aug.

Kalnay, E. (2003), *Atmospheric Modeling, Data Assimilation and Predictability*, 341 pp., Cambridge Univ. Press, Cambridge, U. K.

Kato, T. (1995), A Box-Lagrangian rain-drop scheme, *J. Meteorol. Soc. Jpn.*, *73*, 241–245.

Kawamoto, K., T. Nakajima, and T. Y. Nakajima (2001), A global determination of cloud microphysics with AVHRR remote sensing, *J. Clim.*, *14*, 2054–2068, doi:10.1175/1520-0442(2001)014<2054:AGDOCM>2.0.CO;2.

Khain, A. P., and I. L. Sednev (1995), Simulation of hydrometeor size spectra evolution by water-water, ice-water and ice-ice interactions, *Atmos. Res.*, *36*, 107–138, doi:10.1016/0169-8095(94)00030-H.

Khain, A. P., and I. Sednev (1996), Simulation of precipitation formation in the eastern Mediterranean coastal zone using a spectral microphysics cloud ensemble model, *Atmos. Res.*, *43*, 77–110, doi:10.1016/S0169-8095(96)00005-1.

Khain, A. P., A. Pokrovsky, and I. Sednev (1999), Some effects of cloud-aerosol interaction on cloud microphysics structure and precipitation formation: Numerical experiments with a spectral microphysics cloud ensemble model, *Atmos. Res.*, *52*, 195–220, doi:10.1016/S0169-8095(99)00027-7.

Khain, A. P., M. Ovtchinnikov, M. Pinsky, A. Plkrovsky, and H. Krugliak (2000), Notes on the state-of-the-art numerical modeling of cloud microphysics, *Atmos. Res.*, *55*, 159–224, doi:10.1016/S0169-8095(00)00064-8.

Khain, A., A. Pokrovsky, M. Pinsky, A. Seifert, and V. Phillips (2004), Simulation of effects of atmospheric aerosols on deep turbulent convective clouds using a spectral microphysics mixed-phase cumulus cloud model. Part I: Model description and possible applications, *J. Atmos. Sci.*, *61*, 2963–2982, doi:10.1175/JAS-3350.1.

Khain, A., D. Rosenfeld, and A. Pokrovsky (2005), Aerosol impact on the dynamics and microphysics of deep convective clouds, *Q. J. R. Meteorol. Soc.*, *131*, 2639–2663, doi:10.1256/qj.04.62.

Khain, A. P., N. BenMoshe, and A. Pokrovsky (2008), Factors determining the impact of aerosols on surface precipitation from clouds: An attempt at classification, *J. Atmos. Sci.*, *65*, 1721–1748.

Kogan, Y. L. (1991), The simulation of a convective cloud in a 3-D model with explicit microphysics. Part I: Model description and sensitivity experiments, *J. Atmos. Sci.*, *48*, 1160–1189, doi:10.1175/1520-0469(1991)048<1160:TSOACC>2.0.CO;2.

Lohmann, U. (2002), A glaciation indirect effect caused by soot aerosols, *Geophys. Res. Lett.*, *29*(4), 1052, doi:10.1029/2001GL014357.

Low, R. D. H. (1969), A generalized equation for the solution effect in droplet growth, *J. Atmos. Sci.*, *26*, 608–611, doi:10.1175/1520-0469(1969)026<0608:AGEFTS>2.0.CO;2.

Lynn, B. H., A. P. Khain, J. Dudhia, D. Rosenfeld, A. Pokrovsky, and A. Seifert (2005a), Spectral (bin) microphysics coupled with a mesoscale Model (MM5). Part I: Model description and first results, *Mon. Weather Rev.*, *133*(1), 44, doi:10.1175/MWR-2840.1.

Lynn, B. H., A. P. Khain, J. Dudhia, D. Rosenfeld, A. Pokrovsky, and A. Seifert (2005b), Spectral (bin) microphysics coupled with a mesoscale model (MM5). Part II: Simulation of a CaPE rain event with a squall line, *Mon. Weather Rev.*, *133*(1), 59, doi:10.1175/MWR-2841.1.

Lynn, B., A. Khain, D. Rosenfeld, and W. L. Woodley (2007), Effects of aerosols on precipitation from orographic clouds, *J. Geophys. Res.*, *112*, D10225, doi:10.1029/2006JD007537.

Menzies, R. T., D. M. Tratt, J. D. Spinhirne, and D. L. Hlavka (2002), Aerosol layers over the Pacific Ocean: Vertical distributions and optical properties as observed by multiwavelength airborne lidars, *J. Geophys. Res.*, *107*(D16), 4292, doi:10.1029/2001JD001196.

Meyers, M. P., P. J. DeMott, and W. R. Cotton (1992), New primary ice-nucleation parameterizations in an explicit cloud model, *J. Appl. Meteorol.*, *31*, 708–721, doi:10.1175/1520-0450(1992)031<0708:NPINPI>2.0.CO;2.

Nakajima, T., and M. D. King (1990), Determination of the optical thickness and effective radius of clouds from reflected solar radiation measurements. Part I: Theory, *J. Atmos. Sci.*, *47*, 1878–1893, doi:10.1175/1520-0469(1990)047<1878:DOTOTA>2.0.CO;2.

Nakajima, T. Y., and T. Nakajima (1995), Wide-area determination of cloud microphysical properties from NOAA AVHRR measurements for FIRE and ASTEX regions, *J. Atmos. Sci.*, *52*, 4043–4059, doi:10.1175/1520-0469(1995)052<4043:WADOCM>2.0.CO;2.

Nakajima, T., M. Tsukamoto, Y. Tsushima, A. Numaguti, and T. Kimura (2000), Modeling of the radiative process in an atmospheric general circulation model, *Appl. Opt.*, *39*, 4869–4878, doi:10.1364/AO.39.004869.

Nakajima, T., et al. (2003), Significance of direct and indirect radiative forcings of aerosols in the East China Sea region, *J. Geophys. Res.*, *108*(D23), 8658, doi:10.1029/2002JD003261.

Nakajima, T. Y., A. Uchiyama, T. Takamura, N. Tsujioka, T. Takemura, and T. Nakajima (2005), Comparisons of warm cloud properties obtained from satellite, ground, and aircraft measurements during APEX intensive observation period in 2000 and 2001, *J. Meteorol. Soc. Jpn.*, *83*, 1085–1095, doi:10.2151/jmsj.83.1085.

Numaguti, A., M. Takahashi, and A. Sumi (1995), Climate system dynamics and modeling, in *Development of an Atmospheric General Circulation Model*, edited by T. Matsuno, pp. 1–27, Cent. for Clim. Syst. Res., Univ. of Tokyo, Tokyo.

Ovtchinnikov, M., and Y. L. Kogan (2000), An investigation of ice production mechanisms using a 3D cloud model with detailed microphysics. Part I: Model description, *J. Atmos. Sci.*, *57*, 2989–3003, doi:10.1175/1520-0469(2000)057<2989:AIOIPM>2.0.CO;2.

Pauluis, O., and S. Garner (2006), Sensitivity of radiative-convective equilibrium simulations to horizontal resolution, *J. Atmos. Sci.*, *63*, 1910–1923, doi:10.1175/JAS3705.1.

Penner, J. E., et al. (2002), A comparison of model- and satellite-derived optical depth and reflectivity, *J. Atmos. Sci.*, *59*, 441–460, doi:10.1175/1520-0469(2002)059<0441:ACOMAS>2.0.CO;2.

Pruppacher, H. R., and J. D. Klett (1997), *Microphysics of Clouds and Precipitation*, 2nd ed., 914 pp., Oxford Univ. Press, New York.

Ramanathan, V., P. J. Crutzen, J. T. Kiehl, and D. Rosenfeld (2001), Aerosols, climate, and the hydrological, *Science*, *294*, 2119–2124, doi:10.1126/science.1064034.

Rogers, R. R., and M. K. Yau (1989), *A Short Course in Cloud Physics*, 3rd ed., 293 pp., Pergamon Press, Oxford, U. K.

Rosenfeld, D. (2000), Suppression of rain and snow by urban and industrial air pollution, *Science*, *287*, 1793–1796, doi:10.1126/science.287.5459.1793.

Rosenfeld, D., and I. M. Lensky (1998), Satellite-based insights into precipitation formation processes in continental and maritime clouds, *Bull. Am. Meteorol. Soc.*, *79*, 2457–2476, doi:10.1175/1520-0477(1998)079<2457:SBIIPF>2.0.CO;2.

Saito, K., T. Kato, H. Eito, and C. Muroi (2001), Documentation of the meteorological research institute/numerical prediction division unified nonhydrostatic model, *Tech. Rep. MRI*, *42*, 133 pp., Meteorol. Res. Inst., Tsukuba, Japan.

Saito, K., et al. (2006), The operational JMA nonhydrostatic mesoscale model, *Mon. Weather Rev.*, *134*(4), 1266, doi:10.1175/MWR3120.1.

Squires, P. (1956), The micro-structure of cumuli in maritime and continental air, *Tellus*, *8*, 443–444.

Stephens, G. L. (1978), Radiation profiles in extended water clouds. II. Parameterization schemes, *J. Atmos. Sci.*, *35*, 2123–2132, doi:10.1175/1520-0469(1978)035<2123:RPIEWC>2.0.CO;2.

Suzuki, K., T. Nakajima, T. Y. Nakajima, and A. Khain (2006), Correlation pattern between effective radius and optical thickness of water clouds simulated by a spectral bin microphysics cloud model, *Sci. Online Lett. Atmos.*, *2*, 116–119, doi:10.2151/sola.2006-030.

Szczodrak, M., P. H. Austin, and P. B. Krummel (2001), Variability of optical depth and effective radius in marine stratocumulus clouds, *J. Atmos. Sci.*, *58*, 2912–2926, doi:10.1175/1520-0469(2001)058<2912:VOODAE>2.0.CO;2.

Takahashi, T. (1974), Numerical simulation of tropical showers, *J. Atmos. Sci.*, *31*, 219–232, doi:10.1175/1520-0469(1974)031<0219:NSOTS>2.0.CO;2.

Takahashi, T., and K. Shimura (2004), Tropical rain characteristics and microphysics in a three-dimensional cloud model, *J. Atmos. Sci.*, *61*, 2817–2845, doi:10.1175/JAS-3294.1.

Takahashi, T., T. Endoh, and G. Wakahama (1991), Vapor diffusional growth of free-falling snow crystals between −3 and −23°C, *J. Meteorol. Soc. Jpn.*, *69*, 15–30.

Takemura, T., H. Okamoto, Y. Maruyama, A. Numaguti, A. Higurashi, and T. Nakajima (2000), Global three-dimensional simulation of aerosol optical thickness distribution of various origins, *J. Geophys. Res.*, *105*(D14), 17,853–17,874, doi:10.1029/2000JD900265.

Takemura, T., T. Nakajima, O. Dubovik, B. N. Holben, and S. Kinne (2002), Single-scattering albedo and radiative forcing of various aerosol species with a global three-dimensional model, *J. Clim.*, *15*, 333–352, doi:10.1175/1520-0442(2002)015<0333:SSAARF>2.0.CO;2.

Takemura, T., T. Nozawa, S. Emori, T. Y. Nakajima, and T. Nakajima (2005), Simulation of climate response to aerosol direct and indirect effects with aerosol transport-radiation model, *J. Geophys. Res.*, *110*, D02202, doi:10.1029/2004JD005029.

Twomey, S. (1974), Pollution and the planetary albedo, *Atmos. Environ.*, *8*, 1251–1256, doi:10.1016/0004-6981(74)90004-3.

Yamada, Y. (2003), Cloud microphysics (in Japanese), in *The JMA Nonhydrostatic Model*, *Annu. Rep.*, *49*, pp. 52–76, Jpn. Meteorol. Agency, Tokyo.

T. Iguchi and T. Nakajima, Center for Climate System Research, University of Tokyo, Kashiwa 277-8568, Japan. (iguchi@ccsr.u-tokyo.ac.jp)

A. P. Khain, Department of Atmospheric Sciences, Institute of Earth Sciences, Hebrew University of Jerusalem, Jerusalem 91904, Israel.

K. Saito, Meteorological Research Institute, Tsukuba 305-0052, Japan.

K. Suzuki, Department of Atmospheric Science, Colorado State University, Fort Collins, CO 80523, USA.

T. Takemura, Research Institute for Applied Mechanics, Kyushu University, Fukuoka 816-8580, Japan.